PAPER • OPEN ACCESS

A distributed resistance inverse method for flow obstacle identification from internal velocity measurements

View the article online for updates and enhancements.

A distributed resistance inverse method for flow obstacle identification from internal velocity measurements

Jorge Aguayo[1,2,*] , **Cristóbal Bertoglio**[2] **and Axel Osses**[1,3]

[1] Mathematical Engineering Department, Faculty of Physical and Mathematical Sciences, Universidad de Chile, Santiago, Chile
[2] Bernoulli Institute, University of Groningen, Groningen, The Netherlands
[3] Center for Mathematical Modeling, Universidad de Chile, Santiago, Chile

E-mail: jaguayo@dim.uchile.cl, c.a.bertoglio@rug.nl and axosses@dim.uchile.cl

Abstract

We present a penalization parameter method for obstacle identification in an incompressible fluid flow for a modified version of the Oseen equations. The proposed method consists in adding a high resistance potential to the system such that some subset of its boundary support represents the obstacle. This allows to work in a fixed domain and highly simplify the solution of the inverse problem via some suitable cost functional. Existence of minimizers and first and second order optimality conditions are derived through the differentiability of the solutions of the Oseen equation with respect to the potential. Finally, several numerical experiments using Navier–Stokes flow illustrate the applicability of the method, for the localization of a bi-dimensional cardiac valve from MRI and ultrasound flow type imaging data.

Keywords: obstacle identification, Navier–Stokes equations, distributed resistance, medical imaging

(Some figures may appear in colour only in the online journal)

*Author to whom any correspondence should be addressed.

1. Introduction

The pathway of blood flow through the heart is regulated by four membrane structures or valves, opening and closing by differential blood pressures. Valvular heart diseases affect 20% of the population. Among them, aortic valve stenosis is the most prevalent one in developed countries [22].

Imaging the 3D shape of the valves is a challenging task. For instance, the aortic valve is very thin (0.5 mm), and therefore its shape can be imaged nowadays using only two modalities: computerized tomography (CT) and transesophageal echocardiography (TEE). Since CT is based on x-rays, it is only used in patients that are selected for valvular replacement in order to obtain the aortic root dimensions for sizing the prosthesis. Such CT images are usually obtained when the valve is closed. Obtaining the image at open valve position requires about 5 times larger radiation dose since the complete cardiac cycle has to be imaged. This is equivalent to the annual recommended total radiation dose (see [27]). TEE is a newer technique, but highly invasive: a wire is inserted through the esophagus of the patient involving a cumbersome procedure. TEE is most of the time applied to monitor valve surgeries (see [19]), and is therefore rarely applied in a diagnostic phase.

Magnetic resonance imaging (MRI) allows to image anatomical structures in a non-invasive and non-ionising way. Unfortunately, the aortic valve geometry is not directly visible with MRI, since the valve thickness is smaller than the image voxel size.

However, visual inspection of 3D Flow MRI imaging (4D flow, see [18]) data sets clearly shows that the valvular shape could be retrieved from the flow pattern in the valve surroundings. This fact motivates to formulate, analyze and numerically assess the inverse problem of inferring rigid obstacles from interior velocity measurements, with the ultimate goal of recovering the shape of cardiac valves at the opening position from velocity images.

Available approaches studied and reported in the mathematical literature are limited to the detection of obstacles in viscous fluid flows using boundary stress measurements, which limits the inverse problem to oversimplified shapes, usually of circular nature [3, 7, 13, 14]. Noteworthy, boundary stress measurements would mean in practice to introduce a catheter close to the valve.

The novelty of this work is the identification of flow obstacles by a distributed resistance inverse method. That is, we propose the incorporation of a large resistance term that allows to model the effect of an obstacle in the viscous fluid. This method reduces the obstacle identification to a simpler potential inverse problem. This idea is inspired by [5, 12, 20], who model cardiac valves using a resistive immerse surface (RIS) given by a Dirac distribution. The problem of using RIS for valve identification would be the need of modifying the discretization of the domain at every iteration of the identification procedure. In contrast, the distributed resistance term that we propose here allows us to work in a fixed domain to solve the valve shape identification problem. This distributed resistance method can also be useful to estimate porosity in porous media flows following Brinkman's law [6, 11].

The paper is structured as follows. In section 2, a parameter identification problem is defined for the Oseen equations (as a linearization of Navier–Stokes equations) adding a resistive potential term with the form $\gamma \boldsymbol{u}$, where $\boldsymbol{u}$ is the velocity field and $\gamma \geqslant 0$ is a function that takes large values in zones where is the obstacle should be located, or 0. In section 3, a proof of the existence of minimizers using appropriate techniques is presented. In sections 4 and 5, first and second order optimality conditions for some suitable cost functions are established, motivating the choice of suitable spaces for the parameter and the feasibility of implementing optimization algorithms to numerically solve this problem. Section 6 presents numerical examples that illustrate the feasibility of the proposed penalty method using Navier–Stokes

equations from a 2D reference case representing the blood flow passing through the aortic valve. We reconstruct the position of the valve from global or local velocity field measurements. For this purpose, synthetic images based on MRI and ultrasound type measurements are used. Finally, conclusions and future work are presented in section 7.

2. Model problem

Consider a non-empty bounded domain $\Omega \subseteq \mathbb{R}^N$, $N \in \{2, 3\}$. The Lebesgue measure of Ω is denoted by $|\Omega|$, which extends to lesser dimension spaces. The norm and seminorms for Sobolev spaces $W^{m,p}(\Omega)$ is denoted by $\|\cdot\|_{m,p,\Omega}$ and $|\cdot|_{m,p,\Omega}$, respectively. For $p = 2$, the norm, seminorms and inner product of the space $W^{m,2}(\Omega) = H^m(\Omega)$ are denoted by $\|\cdot\|_{m,\Omega}$, $|\cdot|_{m,\Omega}$ and $(\cdot, \cdot)_{m,\Omega}$, respectively. Also, $\|\cdot\|_{\infty,\Omega}$ denotes the norm of $L^\infty(\Omega)$. The spaces $\boldsymbol{H}^m(\Omega)$ and $\boldsymbol{W}^{m,p}(\Omega)$ are defined by $\boldsymbol{H}^m(\Omega) = [H^m(\Omega)]^N$ and $\boldsymbol{W}^{m,p}(\Omega) = [W^{m,p}(\Omega)]^N$. The notation for norms, seminorms and inner products will be extended from $W^{m,p}(\Omega)$ or $H^m(\Omega)$.

Consider $\alpha > 0$, $\nu > 0$, $s \geqslant 0$, $M > 0$, Ω with a Lipschitz boundary $\partial\Omega = \Gamma_{\mathrm{D}} \cup \Gamma_N$ such that $\mathrm{int}(\Gamma_{\mathrm{D}}) \cap \mathrm{int}(\Gamma_N) = \emptyset$, an open subset $\omega \subseteq \Omega$, $\boldsymbol{u}_{\mathrm{R}} \in \boldsymbol{H}^1(\omega)^d$, $\boldsymbol{u}_{\mathrm{D}} \in \boldsymbol{H}^{1/2}(\Gamma_{\mathrm{D}})$ and $\boldsymbol{a} \in \boldsymbol{W}^{1,\infty}(\Omega)$ such that $\mathrm{div}\,\boldsymbol{a} = 0$ and $\boldsymbol{a} \cdot \boldsymbol{n} \geqslant 0$ on Γ_N, where $\boldsymbol{n}$ is the outer normal vector. The model problem is defined by

$$\text{minimize} \quad J(\gamma, \boldsymbol{u}) = \frac{1}{2}\|\boldsymbol{u} - \boldsymbol{u}_{\mathrm{R}}\|_{0,\omega}^2 + \frac{\alpha}{2}\|\gamma\|_{s,\Omega}^2 \tag{1}$$

$$
\begin{aligned}
\text{subject to} \quad -\nu \triangle \boldsymbol{u} + (\nabla\boldsymbol{u})\boldsymbol{a} + \nabla p + \gamma\boldsymbol{u} &= \boldsymbol{0} && \text{in } \Omega \\
\mathrm{div}\,\boldsymbol{u} &= 0 && \text{in } \Omega \\
\boldsymbol{u} &= \boldsymbol{u}_{\mathrm{D}} && \text{on } \Gamma_{\mathrm{D}} \\
-\nu\frac{\partial\boldsymbol{u}}{\partial\boldsymbol{n}} + p\boldsymbol{n} &= \boldsymbol{0} && \text{on } \Gamma_N \\
\boldsymbol{u} \in \boldsymbol{H}^1(\Omega)\,, \gamma \in H^s(\Omega) & \\
0 \leqslant \gamma \leqslant M \quad \text{a.e. in } \Omega. &
\end{aligned}
\tag{2}
$$

The modified version of Oseen equations given by equation (2) models the velocity $\boldsymbol{u}$ and pressure p of a fluid that passes through the control volume Ω. The term $\gamma\boldsymbol{u}$, with $\gamma \geqslant 0$, represents the distributed resistance that Ω imposes to the fluid. A zero value of γ represents that the fluid follows the Oseen equations. As the γ values increases in a certain area, the magnitude of $\boldsymbol{u}$ tends to decrease to 0. According to Brinkman's law [6, 11], $1/\gamma$ is an indicator of permeability. The media is completely permeable when $\gamma = 0$, while γ tends to $+\infty$ in zones where there are obstacles. Bounded values of γ model porous media, where porosity decreases as γ increases.

In order to simplifying the analysis of this problem, an equivalent formulation with homogeneous Dirichlet boundary condition is proposed. Let $\boldsymbol{G} \in \boldsymbol{H}^1(\Omega)$ such that $\boldsymbol{G} = \boldsymbol{u}_{\mathrm{D}}$ on Γ_{D}. Taking $\boldsymbol{v} = \boldsymbol{u} - \boldsymbol{G}$, $\boldsymbol{f} = \nu \triangle \boldsymbol{G} - (\nabla\boldsymbol{G})\boldsymbol{a} - \gamma\boldsymbol{G}$ in $\boldsymbol{H}^{-1}(\Omega)$, $g = -\mathrm{div}\,\boldsymbol{G}$ in $L^2(\Omega)$ and $\boldsymbol{h} = \nu\frac{\partial\boldsymbol{G}}{\partial\boldsymbol{n}}$ in $\boldsymbol{H}^{1/2}(\Gamma_N)$, the model problem can be written in a new equivalent form.

$$\text{minimize} \quad J(\gamma, \boldsymbol{v}) = \frac{1}{2}\|\boldsymbol{v} + \boldsymbol{G} - \boldsymbol{u}_{\mathrm{R}}\|_{0,\omega}^2 + \frac{\alpha}{2}\|\gamma\|_{s,\Omega}^2 \tag{3}$$

$$\text{subject to} \quad -\nu \triangle v + (\nabla v)a + \nabla p + \gamma v = f \quad \text{in } H^{-1}(\Omega)$$

$$\text{div } v = g \quad \text{in } \Omega$$

$$v = 0 \quad \text{on } \Gamma_D$$

$$-\nu \frac{\partial v}{\partial n} + pn = h \quad \text{on } \Gamma_N \tag{4}$$

$$v \in H^1(\Omega), \gamma \in H^s(\Omega)$$

$$0 \leqslant \gamma \leqslant M \quad \text{a.e. in } \Omega.$$

Remark 1. The boundary condition imposed in Γ_N strongly depends of $a \cdot n \geqslant 0$, but that hypothesis can be restrictive for some existing phenomena in the applied case. For example, if a vortex crosses the outlet, there may be a region where the flow returns to the domain. To overcome this problem, the so called 'backflow' stabilization techniques [8] can be applied. For example, directional do-nothing condition can be used for this problem. This condition verifies

$$-\nu \frac{\partial u}{\partial n} + pn + \frac{1}{2}(a \cdot n)_- u = 0,$$

where $(x)_- = \min\{x, 0\}$. For this case, the existence of a solution of the Oseen equations is verified [10].

3. Existence of solution

The demonstration of the existence of an optimal solution presented follows the same scheme as [4]. A first step is to introduce some helpful notations.

Definition 2. Let $s \geqslant 0$. The set of admissible parameter functions is defined by

$$\mathcal{A} = \{\gamma \in H^s(\Omega) \, | \, 0 \leqslant \gamma \leqslant M\}.$$

Definition 3. The space $H^1_{\Gamma_D}(\Omega)$, subspace of $H^1(\Omega)$, is defined by

$$H^1_{\Gamma_D}(\Omega) = \{v \in H^1(\Omega) \, | \, v = 0 \quad \text{on} \quad \Gamma_D\}.$$

Definition 4. Let $\gamma \in L^\infty(\Omega)$, the map $A : L^\infty(\Omega) \to H^1_{\Gamma_D}(\Omega) \times L^2_0(\Omega)$ is defined by $A(\gamma) = [A_1(\gamma), A_2(\gamma)] = [v, p]$, where $v \in H^1_{\Gamma_D}(\Omega)$ and $p \in L^2_0(\Omega)$ are the unique variational solutions of the problem (4). In what follows, it is denoted $\mathcal{H} = H^1_{\Gamma_D}(\Omega) \times L^2_0(\Omega)$, which is a Banach space behind the norm

$$\|[v, p]\|_{\mathcal{H}} = \nu|v|_{1,\Omega} + \|p\|_{0,\Omega}.$$

Remark 5. It is possible to ensure that A is well defined, because (4) has an unique solution for every $\gamma \in \mathcal{A}$ (see lemma 5.8 on [23]). Futhermore, there exists a constant $C > 0$, independent of γ, ν, u_D and G, such that

$$\nu|v|^2_{1,\Omega} + (\gamma v, v)_{0,\Omega} \leqslant C \max\left\{\nu, \frac{\|a\|^2_\infty}{\nu}, \|\gamma\|_{\infty,\Omega}\right\} \|G\|^2_{1,\Omega}$$

$$\|p\|^2_{0,\Omega} \leqslant C \max\left\{\nu, \|a\|_{\infty,\Omega}, \frac{\|a\|^2_{\infty,\Omega}}{\nu}, \|\gamma\|_{\infty,\Omega}\right\} \|G\|_{1,\Omega}.$$

The uniformly boundedness of $\|v\|_{1,\Omega}$ and $\|p\|_{0,\Omega}$ are obtained because $\|\gamma\|_{\infty,\Omega} \leqslant M$.

Theorem 6. *Problem* (3) *has at least one solution* $\gamma^* \in \mathcal{A}$ *with optimal states* $A(\gamma^*) = [v^*, p^*]$, *i.e.*

$$(\forall\, \gamma \in \mathcal{A})\ J(\gamma, A_1(\gamma)) \geqslant J\left(\gamma^*, v^*\right).$$

Proof. First, $J(\gamma) = J(\gamma, A(\gamma))$ is bounded below by 0 and

$$(\forall\, \gamma \in \mathcal{A})\ J(\gamma) \geqslant \frac{\alpha}{2}\|\gamma\|_{s,\Omega}^2.$$

Thus, $m = \inf\limits_{\gamma \in \mathcal{A}} J(\gamma)$ is well defined. Let $\{\gamma_n\}_{n\in\mathbb{N}} \subseteq \mathcal{A}$ and $\{[v_n, p_n]\}_{n\in\mathbb{N}} \subseteq \boldsymbol{H}^1_{\Gamma_{\mathrm{D}}}(\Omega) \times L^2_0(\Omega)$ such that $A(\gamma_n) = [v_n, p_n]$, $\{J(\gamma_n)\}$ is decreasing and $J(\gamma_n) \to m$. It is clear that

$$(\forall\, n \in \mathbb{N})\, J(\gamma_n) \leqslant J(\gamma_1).$$

Then, $\{\gamma_n\}_{n\in\mathbb{N}}$ is uniformly bounded in $H^s(\Omega)$. Since $\mathcal{A}$ is weakly closed, there exists a subsequence (denoted by $\{\gamma_n\}_{n\in\mathbb{N}}$) such that $\gamma_n \rightharpoonup \gamma^*$ in $H^s(\Omega)$, with $\gamma^* \in \mathcal{A}$. In particular, $\gamma_n \rightharpoonup \gamma^*$ in $L^2(\Omega)$. By the same way, $\{v_n\}_{n\in\mathbb{N}}$ and $\{p_n\}_{n\in\mathbb{N}}$ are also uniformly bounded (see remark 5) on $\boldsymbol{H}^1_{\Gamma_{\mathrm{D}}}(\Omega)$ and $L^2_0(\Omega)$, respectively. Applying the Sobolev embedding theorem (see section 6.6 in [16]), there exists a subsequence (also denoted by $\{v_n\}_{n\in\mathbb{N}}$) such that $v_n \rightharpoonup v^*$ weakly in $\boldsymbol{H}^1_{\Gamma_{\mathrm{D}}}(\Omega)$, with $v^* \in \boldsymbol{H}^1_{\Gamma_{\mathrm{D}}}(\Omega)$, and $v_n \to v^*$ in $\boldsymbol{L}^p(\Omega)$ for $p \in [2,6)$ when $N \geqslant 3$, or for $p \geqslant 2$ when $N = 2$. In particular,

$$v_n \to v^* \quad \text{in} \quad \boldsymbol{L}^4(\Omega) \quad \text{and} \quad \boldsymbol{L}^2(\Omega).$$

Let $w \in \boldsymbol{H}^1_{\Gamma_{\mathrm{D}}}(\Omega)$. Since $d \in \{2,3\}$, then $w \in \boldsymbol{L}^4(\Omega)$. Later, $v_n \cdot w \to v^* \cdot w$ in $L^2(\Omega)$ and $(\nabla v_n)a \rightharpoonup (\nabla v)a$ weakly in $L^2(\Omega)$. Thus, for every $w \in \boldsymbol{H}^1_{\Gamma_{\mathrm{D}}}(\Omega)$

$$(\gamma_n v_n, w)_{0,\Omega} \to \left(\gamma^* v^*, w\right)_{0,\Omega}\ ((\nabla v_n)a, w)_{0,\Omega} \to \left((\nabla v^*)a, w\right)_{0,\Omega}.$$

Repeating this argument, there exists a subsequence also denoted by $\{p_n\}_{n\in\mathbb{N}}$ such that

$$p_n \rightharpoonup p^* \quad \text{in } L^2_0(\Omega).$$

In conclusion, $(v^*, p^*) \in \mathcal{H}$ is the variational solution of equation (4). In other words, $A(\gamma^*) = [v^*, p^*]$. Now, γ^* is optimal. Indeed,

$$
\begin{aligned}
m &= \lim_{n\to\infty} J(\gamma_n) \\
&\geqslant \lim_{n\to\infty} \frac{1}{2}\|v_n + G - u_{\mathrm{R}}\|_{0,\omega}^2 + \frac{\alpha}{2}\liminf_{n\to\infty}\|\gamma_n\|_{s,\Omega}^2 \\
&\geqslant \frac{1}{2}\|v^* + G - u_{\mathrm{R}}\|_{0,\omega}^2 + \frac{\alpha}{2}\|\gamma^*\|_{s,\Omega}^2 = J(\gamma^*) \geqslant m.
\end{aligned}
$$

Hence, $J(\gamma, A_1(\gamma)) \geqslant J(\gamma^*, v^*)$ for every $\gamma \in \mathcal{A}$, proving this theorem. □

4. First order necessary optimality condition

In order to implement a descent method to numerically solve this problem, it is necessary to establish the differentiability of functional J. However, this directly depends on the

differentiability of map A. From this result, it is possible to establish necessary optimality conditions.

Theorem 7.   *The map A is Fréchet-differentiable. For each $\gamma, \gamma_1 \in \mathcal{A}$, if $A(\gamma) = [v, p]$, then the Fréchet derivative $A'(\gamma)[\gamma_1] = \left[v'_1, p'_1\right]$ can be described by the weak solution of the following problem*

$$
\begin{aligned}
-\nu \triangle v'_1 + \left(\nabla v'_1\right) a + \nabla p'_1 + \gamma v'_1 &= -\gamma_1 (v + G) && \text{in } \Omega \\
\operatorname{div} v'_1 &= 0 && \text{in } \Omega \\
v'_1 &= \mathbf{0} && \text{on } \Gamma_D \\
-\nu \frac{\partial v'_1}{\partial n} + p'_1 n &= \mathbf{0} && \text{on } \Gamma_N.
\end{aligned}
\tag{5}
$$

Proof.   See appendix A   □

Defining $B(v) = \frac{1}{2}\|v + G - u_R\|^2_{0,\omega}$ and $C(\gamma) = \frac{\alpha}{2}\|\gamma\|^2_{s,\Omega}$, an expression for Frechét derivatives of B and C is given by

$$
B'(v)[w] = (v + G - u_R, w)_{0,\omega} \quad C'(\gamma)[\beta] = \alpha(\gamma, \beta)_{s,\Omega}.
$$

Applying chain rule, it is obtained that

$$
\begin{aligned}
J'(\gamma)[\gamma_1] &= B'(v)\left[A'_1(\gamma)[\gamma_1]\right] + C'(\gamma)[\gamma_1] \\
&= \left(v + G - u_R, v'_1\right)_{0,\omega} + \alpha(\gamma, \gamma_1)_{s,\Omega}.
\end{aligned}
$$

In order to reduce this expression, the following definition is introduced similarly to [1].

Definition 8.   Let $\gamma \in \mathcal{A}$ and $A(\gamma) = [v, p]$. The adjoint states $A^*(\gamma) = [\varphi, \xi]$ are defined as the unique weak solution of the problem

$$
\begin{aligned}
-\nu \triangle \varphi - (\nabla \varphi) a + \nabla \xi + \gamma \varphi &= \chi_\omega (v + G - u_R) && \text{in } \Omega \\
\operatorname{div} \varphi &= 0 && \text{in } \Omega \\
\varphi &= \mathbf{0} && \text{on } \Gamma_D \\
-\nu \frac{\partial \varphi}{\partial n} + \xi n - (a \cdot n) \varphi &= \mathbf{0} && \text{on } \Gamma_N.
\end{aligned}
\tag{6}
$$

where χ_ω is the indicator function of ω.

Using this definition, it is possible to rewrite $J'(\gamma_1)$ depending of the adjoint state. That expression is simpler to analyze, since it depends on the adjoint state, allowing a simple form of a first order optimality condition using a variational inequality.

Theorem 9.   *Let $\gamma, \gamma_1 \in \mathcal{A}$ and $s \geqslant 0$. Then,*

$$
J'(\gamma)[\gamma_1] = -(\gamma_1 (v + G), \varphi)_{0,\Omega} + \alpha(\gamma, \gamma_1)_{s,\Omega},
$$

where $A(\gamma) = [v, p]$. If $\gamma^* \in \mathcal{A}$ is an optimal for problem (3), then

$$
(\forall \gamma \in \mathcal{A}) - \left((\gamma - \gamma^*)(v^* + G), \varphi\right)_{0,\Omega} + \alpha(\gamma^*, \gamma - \gamma^*)_{s,\Omega} \geqslant 0
$$

where $A(\gamma^*) = [v^*, p^*]$ and $A^*(\gamma^*) = [\varphi, \xi]$ are the states and adjoint states of γ^*, respectively.

Proof.   First, using integration by parts with the adjoint states $[\varphi, \xi]$ as tests functions, it is obtained that

$$-\nu \int_{\Omega} \triangle \, \boldsymbol{v}'_1 \cdot \boldsymbol{\varphi} \, \mathrm{d}\boldsymbol{x} = -\nu \int_{\Omega} \triangle \, \boldsymbol{\varphi} \cdot \boldsymbol{v}'_1 \, \mathrm{d}\boldsymbol{x} + \int_{\partial\Omega} \boldsymbol{\varphi} \cdot \left(-\nu \frac{\partial \boldsymbol{v}'_1}{\partial \boldsymbol{n}}\right) - \boldsymbol{v}'_1 \cdot \left(-\nu \frac{\partial \boldsymbol{\varphi}}{\partial \boldsymbol{n}}\right) \mathrm{d}S$$

$$\int_{\Omega} \left[(\nabla \boldsymbol{v}'_1) \, \boldsymbol{a} \right] \cdot \boldsymbol{\varphi} \, \mathrm{d}\boldsymbol{x} = -\int_{\Omega} \left[(\nabla \boldsymbol{a}) \, \boldsymbol{v}'_1 \right] \cdot \boldsymbol{\varphi} \, \mathrm{d}\boldsymbol{x} + \int_{\partial\Omega} (\boldsymbol{a} \cdot \boldsymbol{n}) \, (\boldsymbol{\varphi} \cdot \boldsymbol{v}'_1) \, \, \mathrm{d}S$$

$$\int_{\Omega} \nabla p'_1 \cdot \boldsymbol{\varphi} \, \, \mathrm{d}\boldsymbol{x} = -\int_{\Omega} p'_1 \, \mathrm{div} \, \boldsymbol{\varphi} \, \mathrm{d}\boldsymbol{x} + \int_{\partial\Omega} \boldsymbol{\varphi} \cdot (p'_1 \boldsymbol{n}) \, \mathrm{d}S$$

$$-\int_{\Omega} \xi \, \mathrm{div} \, \boldsymbol{v}'_1 \, \mathrm{d}\boldsymbol{x} = \int_{\Omega} \nabla \xi \cdot \boldsymbol{v}'_1 \, \mathrm{d}\boldsymbol{x} - \int_{\partial\Omega} \boldsymbol{v}'_1 \cdot (\xi \boldsymbol{n}) \, \mathrm{d}S.$$

Then,

$$-(\gamma_1 \, (\boldsymbol{v} + \boldsymbol{G}) \, , \boldsymbol{\varphi})_{0,\Omega} = -\nu \int_{\Omega} \triangle \, \boldsymbol{v}'_1 \cdot \boldsymbol{\varphi} \, \mathrm{d}\boldsymbol{x} + \int_{\Omega} \left[(\nabla \boldsymbol{v}'_1) \, \boldsymbol{a} \right] \cdot \boldsymbol{\varphi} \, \mathrm{d}\boldsymbol{x}$$

$$+ \int_{\Omega} \nabla p'_1 \cdot \boldsymbol{\varphi} \, \, \mathrm{d}\boldsymbol{x} + \int_{\Omega} \gamma \boldsymbol{v}'_1 \cdot \boldsymbol{\varphi} \, \mathrm{d}\boldsymbol{x} - \int_{\Omega} \xi \, \mathrm{div} \, \boldsymbol{v}'_1 \, \, \mathrm{d}\boldsymbol{x}$$

$$= -\nu \int_{\Omega} \triangle \, \boldsymbol{\varphi} \cdot \boldsymbol{v}'_1 \, \mathrm{d}\boldsymbol{x} - \int_{\Omega} [(\nabla \boldsymbol{\varphi}) \, \boldsymbol{a}] \cdot \boldsymbol{v}'_1 \, \mathrm{d}\boldsymbol{x} + \int_{\Omega} \nabla \xi \cdot \boldsymbol{v}'_1 \, \, \mathrm{d}\boldsymbol{x}$$

$$+ \int_{\Omega} \gamma \boldsymbol{v}'_1 \cdot \boldsymbol{\varphi} \, \mathrm{d}\boldsymbol{x} - \int_{\Omega} p'_1 \, \mathrm{div} \, \boldsymbol{\varphi} \, \mathrm{d}\boldsymbol{x} + \int_{\Gamma_N} \boldsymbol{\varphi} \cdot \left(-\nu \frac{\partial \boldsymbol{v}'_1}{\partial \boldsymbol{n}} + p'_1 \boldsymbol{n}\right)$$

$$- \int_{\Gamma_N} \boldsymbol{v}'_1 \cdot \left(-\nu \frac{\partial \boldsymbol{\varphi}}{\partial \boldsymbol{n}} + \xi \boldsymbol{n} - (\boldsymbol{a} \cdot \boldsymbol{n}) \, \boldsymbol{\varphi}\right) \mathrm{d}S$$

$$= -\nu \int_{\Omega} \triangle \, \boldsymbol{\varphi} \cdot \boldsymbol{v}'_1 \, \mathrm{d}\boldsymbol{x} - \int_{\Omega} \left[(\nabla \boldsymbol{v}'_1) \, \boldsymbol{a} \right] \cdot \boldsymbol{\varphi} \, \mathrm{d}\boldsymbol{x} + \int_{\Omega} \nabla \xi \cdot \boldsymbol{v}'_1 \, \, \mathrm{d}\boldsymbol{x}$$

$$+ \int_{\Omega} \gamma \boldsymbol{v}'_1 \cdot \boldsymbol{\varphi} \, \mathrm{d}\boldsymbol{x} - \int_{\Omega} p'_1 \, \mathrm{div} \, \boldsymbol{\varphi} \, \mathrm{d}\boldsymbol{x}$$

$$= \left((\boldsymbol{v} + \boldsymbol{G} - \boldsymbol{u}_{\mathrm{D}}) \, , \boldsymbol{v}'_1 \right)_{0,\omega}$$

Thus,

$$J'(\gamma) [\gamma_1] = -(\gamma_1 \, (\boldsymbol{v} + \boldsymbol{G}) \, , \boldsymbol{\varphi})_{0,\Omega} + \alpha(\gamma, \gamma_1)_{s,\Omega}$$

Later, if $\gamma^* \in \mathcal{A}$ is optimal for the problem, then

$$(\forall \, \gamma \in \mathcal{A}) \quad J(\gamma) \geqslant J(\gamma^*),$$

Finally, it is obtained that

$$J'(\gamma^*) [\gamma - \gamma^*] = \lim_{\varepsilon \to 0^+} \frac{J(\gamma^* + \varepsilon \, (\gamma - \gamma^*)) - J(\gamma^*)}{\varepsilon} \geqslant 0,$$

proving this theorem.   □

5. Second order sufficient optimality condition

The stability results of the optimization algorithms depend, for the most part, on the existence of the second derivative of J. Likewise, it is possible to establish second order sufficient optimality conditions.

In first place, it is necessary to introduce new forms of embedding inequalities.

Theorem 10. *There exists a constant $q^* > 2$, dependent only of Ω, such that for each $p \in [2, q^*]$ there exists a constant $C > 0$, dependent only of Ω, M, ν and p such that*

$$\|v\|_{1,p,\Omega} \leqslant C \|G\|_{-1,p,\Omega},$$

where $G \in W^{-1,p}(\Omega)$ (the dual of $W_0^{1,q}(\Omega)$) is defined by

$$\left(\forall\, w \in W_0^{1,q}(\Omega)\right) \quad \langle G(v), w \rangle = \langle f, w \rangle_{H^{-1}(\Omega), H^1(\Omega)} + (h, w)_{0, \Gamma_N}$$

with $q \geqslant 2$ such that $\frac{1}{p} + \frac{1}{q} = 1$.

Proof. See theorem 1 in [21]. $\qquad\square$

Remark 11. The hypotheses $u_R \in L^\infty(\omega)$ and $u_D \in L^\infty(\Gamma_D)$ appear frequently. Assuming $u_R \in L^\infty(\omega)$ and $u_D \in L^\infty(\Gamma_D)$, it is clear that $G \in W^{1,\infty}(\Omega)$. Then, there exists a constant $C_p > 0$, depending only of p and Ω, such that

$$\|G\|_{-1,p,\Omega} \leqslant C_p \max\left\{\nu, \|a\|_{\infty,\Omega}, \|\gamma\|_{\infty,\Omega}\right\} \|G\|_{1,\infty,\Omega}.$$

Futhermore, using theorem 10,

$$\|v\|_{1,p,\Omega} \leqslant C C_p \max\left\{\nu, \|a\|_{\infty,\Omega}, M\right\} \|G\|_{1,\infty,\Omega}.$$

So, $\|v\|_{1,p,\Omega}$ is uniformly bounded for each $p \in [2, q^*]$. Also, theorem 1 in [21] allows us to be more precise about the asymptotic behavior of q^*. Indeed, if the value of $\|\gamma\|_{\infty,\Omega}$ increases, q^* decreases to 2.

Lemma 12. *Let $s > 0$ and $p \in [1, N]$.*

(a) If $N > sp$, then the embedding from $W^{s,p}(\Omega)$ to $L^r(\Omega)$ is continuous for $r \in \left[p, \frac{d}{d-sp}\right]$.
(b) If $N = sp$, then the embedding from $W^{s,p}(\Omega)$ to $L^r(\Omega)$ is continuous for $r \in [p, +\infty)$.

Proof. See section 6.6 in [16] $\qquad\square$

Remark 13. Using this embedding result with $s \geqslant \frac{N}{q^*}$ and $p = 2$, lemma 12 can be written by

(a) If $q^* > 2$, then the embedding from $H^{d/q^*}(\Omega)$ to $L^r(\Omega)$ is compact for $r \in \left[2, \frac{1}{\frac{1}{p} - \frac{1}{q^*}}\right]$.
(b) If $q^* = 2$, then the embedding from $H^{d/q^*}(\Omega)$ to $L^r(\Omega)$ is compact for $r \in [2, +\infty)$.

Then, for $2 \leqslant p \leqslant \frac{1}{\frac{1}{2} - \frac{1}{q^*}}$ there exists $C > 0$ such that

$$(\forall\, \gamma \in \mathcal{A})\, \|\gamma\|_{0,p,\Omega} \leqslant C \|\gamma\|_{s,\Omega}.$$

In order to establish and prove second order optimality conditions, a first step is to show that the map A is twice Fréchet-differentiable.

Theorem 14. *The map $\gamma \longmapsto A'(\gamma)[\gamma_1]$ from $L^{\infty}(\Omega)$ to $\mathcal{H}$ for each $\gamma_1 \in \mathcal{A}$ is Fréchet-differentiable. Let $\gamma, \gamma_1, \gamma_2 \in\in \mathcal{A}$, the Fréchet derivative of $A'(\gamma)[\gamma_1]$ on γ_2 direction is given by $A''(\gamma)[\gamma_1, \gamma_2] = [\boldsymbol{v}'', p'']$, where $[\boldsymbol{v}'', p'']$ is the unique weak solution of the problem*

$$
\begin{aligned}
-\nu \triangle \boldsymbol{v}'' + \left(\nabla \boldsymbol{v}''\right)\boldsymbol{a} + \nabla p'' + \gamma \boldsymbol{v}'' &= -\left(\gamma_2 \boldsymbol{v}'_1 + \gamma_1 \boldsymbol{v}'_2\right) && \text{in } \Omega \\
\operatorname{div} \boldsymbol{v}'' &= 0 && \text{in } \Omega \\
\boldsymbol{v}'' &= \boldsymbol{0} && \text{on } \Gamma_{\mathrm{D}} \\
-\nu \frac{\partial \boldsymbol{v}''}{\partial \boldsymbol{n}} + p'' \boldsymbol{n} &= \boldsymbol{0} && \text{on } \Gamma_N.
\end{aligned}
\tag{7}
$$

and $A'(\gamma)\gamma_j = [\boldsymbol{v}'_j, p'_j]$, for $j \in \{1, 2\}$.

Proof. See appendix B $\qquad\qquad\square$

Let $\gamma, \gamma_1, \gamma_2 \in \mathcal{A}$. An expression for the Fréchet second derivative of $J(\gamma)$ on directions γ_1 and γ_2 is given by

$$
\begin{aligned}
J''(\gamma)[\gamma_1, \gamma_2] &= B''(A(\gamma))\left[A'_1(\gamma_1), A'(\gamma_2)\right] + B'((A(\gamma)))\left[A''_1(\gamma)[\gamma_1, \gamma_2]\right] \\
&\quad + C''(\gamma)[\gamma_1, \gamma_2] \\
&= \left(\boldsymbol{v}'_1, \boldsymbol{v}'_2\right)_{0,\Omega} + \left(\boldsymbol{v} + \boldsymbol{G} - \boldsymbol{u}_{\mathrm{D}}, \boldsymbol{v}''\right)_{0,\omega} + \alpha(\gamma_1, \gamma_2)_{s,\Omega},
\end{aligned}
$$

where, reasoning as in the proof of theorem 9,

$$
\left(\boldsymbol{v} + \boldsymbol{G} - \boldsymbol{u}_{\mathrm{D}}, \boldsymbol{v}''\right)_{0,\omega} = -\left(\gamma_1 \boldsymbol{v}'_2 + \gamma_2 \boldsymbol{v}'_1, \boldsymbol{\varphi}\right)_{0,\Omega}.
$$

In consequence,

$$
\begin{aligned}
J''(\gamma)[\gamma_1, \gamma_2] &= B''(A(\gamma))\left[A'_1(\gamma_1), A'(\gamma_2)\right] + B'((A(\gamma)))\left[A''_1(\gamma)[\gamma_1, \gamma_2]\right] \\
&\quad + C''(\gamma)[\gamma_1, \gamma_2] \\
&= \left(\boldsymbol{v}'_1, \boldsymbol{v}'_2\right)_{0,\Omega} - \left(\gamma_1 \boldsymbol{v}'_2 + \gamma_2 \boldsymbol{v}'_1, \boldsymbol{\varphi}\right)_{0,\Omega} + \alpha(\gamma_1, \gamma_2)_{s,\Omega}.
\end{aligned}
$$

In what follows, a second order optimality condition is proved. For this, a series of technical results are required. Consider r such that $\frac{1}{q^*} + \frac{1}{r} = \frac{1}{2}$. For $\gamma, \gamma_1, \gamma_2, h \in \mathcal{A}$, consider $A(\gamma) = [\boldsymbol{v}, p]$, $A(\gamma + h) = [\boldsymbol{v}_h, p_h]$, with respective adjoint states $[\boldsymbol{\varphi}, \xi]$ and $[\boldsymbol{\varphi}_h, \xi_h]$, $A'(\gamma)[\gamma_k] = [\boldsymbol{v}'_k, p'_k]$ and $[\boldsymbol{v}'_{h,k}, p'_{h,k}] = A'(\gamma + h)[\gamma_k]$ for $k \in \{1, 2\}$. Using this, it is possible to obtain the following estimations.

Lemma 15. *For each $q \in [2, q^*]$, there exists $C > 0$, independent of $\boldsymbol{v}, \gamma, \gamma_1, \gamma_2$ and h such that $\|\boldsymbol{v}_h - \boldsymbol{v}\|_{1,q,\Omega} \leqslant C\|h\|_{\infty,\Omega}$,*

Proof. Subtracting the equations of $A(\gamma + h)$ and $A(\gamma)$, it is obtained

$$
-\nu \triangle (\boldsymbol{v}_h - \boldsymbol{v}) + [\nabla (\boldsymbol{v}_h - \boldsymbol{v})]\boldsymbol{a} + \nabla (p_h - p) + \gamma (\boldsymbol{v}_h - \boldsymbol{v}) = -h(\boldsymbol{G} + \boldsymbol{v}_h).
$$

Using theorem 10 twice and triangular inequality, there exist $c_1, c_2 > 0$ such that

$$
\begin{aligned}
\|\boldsymbol{v}\|_{1,q,\Omega} &\leqslant c_1 \|h(\boldsymbol{G} + \boldsymbol{v}_h)\|_{-1,q,\Omega} \\
&\leqslant c_1 \|h\|_{\infty,\Omega} \|(\boldsymbol{G} + \boldsymbol{v}_h)\|_{1,q,\Omega} \\
&\leqslant c_2 \|h\|_{\infty,\Omega} \|\boldsymbol{G}\|_{1,\infty,\Omega}.
\end{aligned}
$$

9

Taking $C = c_2\|\boldsymbol{G}\|_{1,\infty,\Omega}$, the estimation is proved. $\qquad\square$

Lemma 16. *Let* $k \in \{1, 2\}$. *There exists* $C > 0$ *independent of* $\boldsymbol{v}, \gamma, \gamma_1, \gamma_2$ *and* h *such that* $\left|\boldsymbol{v}'_{k,h}\right|_{1,\Omega} \leqslant C\|\gamma_k\|_{s,\Omega}$.

Proof. First, testing the equation of $\boldsymbol{v}'_{h,k}$ with $\boldsymbol{v}'_{h,k}$ and applying Friedichs–Poincaré and Hölder inequalities, there exists a constant $c_1 > 0$ such that

$$\nu\left|\boldsymbol{v}'_{h,k}\right|_{1,\Omega} \leqslant c_1\left\|\gamma_k\left(\boldsymbol{G} + \boldsymbol{v}_{k,h}\right)\right\|_{0,\Omega}$$

$$\leqslant c_1\|\gamma_k\|_{0,r,\Omega}\left\|\left(\boldsymbol{G} + \boldsymbol{v}_{k,h}\right)\right\|_{0,q^*,\Omega}$$

From remark 11, $\left\|\left(\boldsymbol{G} + \boldsymbol{v}_{k,h}\right)\right\|_{0,q^*,\Omega}$ is uniformly bounded by $c_2 > 0$. Also, due to $r = \frac{1}{\frac{1}{2} - \frac{1}{q^*}}$, remark 13 points out that there exists $c_3 > 0$ such that $\|\gamma_k\|_{0,r,\Omega} \leqslant c_3\|\gamma_k\|_{s,\Omega}$. In conclusion,

$$\nu\left|\boldsymbol{v}'_{h,k}\right|_{1,\Omega} \leqslant c_2 c_3\|\gamma_k\|_{s,\Omega},$$

proving this estimation. $\qquad\square$

Lemma 17. *There exists* $C > 0$ *such that*

$$\left|\left(\boldsymbol{v}'_{h,1} - \boldsymbol{v}'_1, \boldsymbol{v}'_2\right)_{0,\Omega}\right| \leqslant C\|\gamma_1\|_{s,\Omega}\|\gamma_2\|_{s,\Omega}\|h\|_{\infty,\Omega}$$

$$\left|\left(\boldsymbol{v}'_{h,1}, \boldsymbol{v}'_{h,2} - \boldsymbol{v}'_2\right)_{0,\Omega}\right| \leqslant C\|h\|_{\infty,\Omega}\|\gamma_1\|_{s,\Omega}\|\gamma_2\|_{s,\Omega}.$$

Proof. Using Cauchy–Schwartz and Friedrichs–Poincaré inequalities, there exist $c_1, c_2 > 0$ such that

$$\left|\left(\boldsymbol{v}'_{h,1} - \boldsymbol{v}'_1, \boldsymbol{v}'_2\right)_{0,\Omega}\right| \leqslant c_1\left|\boldsymbol{v}'_2\right|_{1,\Omega}\left|\boldsymbol{v}'_{h,1} - \boldsymbol{v}'_1\right|_{1,\Omega} \leqslant c_2\|\gamma_2\|_{s,\Omega}\left|\boldsymbol{v}'_{h,1} - \boldsymbol{v}'_1\right|_{1,\Omega}.$$

Using previous lemmas, Friedrichs–Poincaré inequality and remark 13, there exist $c_3, c_4, c_5, c_6 > 0$ such that

$$\nu\left|\boldsymbol{v}'_{h,1} - \boldsymbol{v}'_1\right|_{1,\Omega} \leqslant c_3\left(\|h\|_{\infty,\Omega}\left|\boldsymbol{v}'_{h,1}\right|_{1,\Omega} + \|\gamma_1\left(\boldsymbol{v}_h - \boldsymbol{v}\right)\|_{1,\Omega}\right)$$

$$\leqslant c_3\left(c_4\|h\|_{\infty,\Omega}\|\gamma_1\|_{s,\Omega} + c_5\|\gamma_1\|_{0,r,\Omega}\|(\boldsymbol{v}_h - \boldsymbol{v})\|_{1,q^*,\Omega}\right)$$

$$\leqslant c_3\left(c_4 + c_6\right)\|h\|_{\infty,\Omega}\|\gamma_1\|_{s,\Omega},$$

concluding that

$$\left|\left(\boldsymbol{v}'_{h,1}, \boldsymbol{v}'_{h,2} - \boldsymbol{v}'_2\right)_{0,\Omega}\right| \leqslant C\|h\|_{\infty,\Omega}\|\gamma_1\|_{s,\Omega}\|\gamma_2\|_{s,\Omega}.$$

The proof of the second inequality is similar. $\qquad\square$

Lemma 18. *Let* $k, j \in \{1, 2\}$, *with* $j \neq k$. *There exists* $C > 0$ *such that*

$$\left|\left(\gamma_j\boldsymbol{v}'_{h,k}, \boldsymbol{\varphi}_h - \boldsymbol{\varphi}\right)_{0,\Omega}\right| \leqslant C\|h\|_{\infty,\Omega}\|\gamma_1\|_{s,\Omega}\|\gamma_2\|_{s,\Omega}.$$

Proof. First, applying Hölder and Friedrichs–Poincaré inequalities, there exist $c_1, c_2 > 0$ such that

$$\left|\left(\gamma_j\boldsymbol{v}'_{h,k}, \boldsymbol{\varphi}_h - \boldsymbol{\varphi}\right)_{0,\Omega}\right| \leqslant c_1\|\gamma_j\|_{0,r,\Omega}\left\|\boldsymbol{v}'_{h,k}\right\|_{1,q^*,\Omega}|\boldsymbol{\varphi}_h - \boldsymbol{\varphi}|_{1,\Omega}$$

$$\leqslant c_2\|\gamma_j\|_{s,\Omega}\|\gamma_k\|_{s,\Omega}|\boldsymbol{\varphi}_h - \boldsymbol{\varphi}|_{1,\Omega},$$

where $\left[\boldsymbol{\varphi}_h - \boldsymbol{\varphi}, \xi_h - \xi\right]$ verifies

$$-\nu \triangle \left(\boldsymbol{\varphi}_h - \boldsymbol{\varphi}\right) - \left[\nabla \left(\boldsymbol{\varphi}_h - \boldsymbol{\varphi}\right)\right] \boldsymbol{a} + \nabla \left(\xi_h - \xi\right) + \gamma \left(\boldsymbol{\varphi}_h - \boldsymbol{\varphi}\right) = \boldsymbol{v}_h - \boldsymbol{v} - h\boldsymbol{\varphi}_h$$

$$\operatorname{div} \left(\boldsymbol{\varphi}_h - \boldsymbol{\varphi}\right) = 0.$$

By repeating the previous procedures, since $|\boldsymbol{\varphi}_h|_{1,\Omega}$ is uniformly bounded, there exist $c_2, c_3 > 0$ such that

$$\nu |\boldsymbol{\varphi}_h - \boldsymbol{\varphi}|_{1,\Omega} \leqslant c_2 \left(\|\boldsymbol{v}_h - \boldsymbol{v}\|_{1,q,\Omega} + \|h\|_{\infty,\Omega} |\boldsymbol{\varphi}_h|_{1,\Omega}\right)$$

$$\leqslant c_3 \|h\|_{\infty,\Omega}.$$

Thus, there exists $C > 0$ such that $\left|\left(\gamma_j \boldsymbol{v}'_{h,k}, \boldsymbol{\varphi}_h - \boldsymbol{\varphi}\right)_{0,\Omega}\right| \leqslant C\|h\|_{\infty,\Omega} |\gamma_j|_{s,\Omega} |\gamma_k|_{s,\Omega}.$ □

Theorem 19. *Let $\gamma, \gamma_1, \gamma_2, h \in L^\infty (\Omega)$. There exists $L > 0$ such that*

$$\left|\left(J'' \left(\gamma + h\right) - J'' \left(\gamma\right)\right) \left[\gamma_1, \gamma_2\right]\right| \leqslant L\|h\|_{\infty,\Omega} |\gamma_1|_{s,\Omega} |\gamma_2|_{s,\Omega}.$$

Proof. Applying triangular inequality, we obtain

$$\left|\left(J'' \left(\gamma + h\right) - J'' \left(\gamma\right)\right) \left[\gamma_1, \gamma_2\right]\right|$$

$$\leqslant \left|\left(\boldsymbol{v}'_{h,1}, \boldsymbol{v}'_{h,2} - \boldsymbol{v}'_2\right)_{0,\Omega}\right| + \left|\left(\boldsymbol{v}'_{h,1} - \boldsymbol{v}'_1, \boldsymbol{v}'_2\right)_{0,\Omega}\right|$$

$$+ \left|\left(\gamma_1 \boldsymbol{v}'_{h,2}, \boldsymbol{\varphi}_h - \boldsymbol{\varphi}\right)_{0,\Omega}\right| + \left|\left(\gamma_1 \left(\boldsymbol{v}'_{h,2} - \boldsymbol{v}'_2\right), \boldsymbol{\varphi}\right)_{0,\Omega}\right|$$

$$+ \left|\left(\gamma_2 \boldsymbol{v}'_{h,1}, \boldsymbol{\varphi}_h - \boldsymbol{\varphi}\right)_{0,\Omega}\right| + \left|\left(\gamma_2 \left(\boldsymbol{v}'_{h,1} - \boldsymbol{v}'_1\right), \boldsymbol{\varphi}\right)_{0,\Omega}\right|,$$

where every term were bounded with estimations of the form $C\|h\|_{\infty,\Omega} |\gamma_1|_{s,\Omega} |\gamma_2|_{s,\Omega}$ (see lemmas 17 and 18). In conclusion, there exists $L > 0$ such that

$$\left|\left(J'' \left(\gamma + h\right) - J'' \left(\gamma\right)\right) \left[\gamma_1, \gamma_2\right]\right| \leqslant L\|h\|_{\infty,\Omega} |\gamma_1|_{s,\Omega} |\gamma_2|_{s,\Omega}.$$

□

Corollary 20. *There exists $L > 0$ such that, for every $\theta \in [0, 1]$*

$$\left|\left(J'' \left(\theta\gamma^* + (1 - \theta)\gamma\right) - J'' \left(\gamma^*\right)\right) \left[\gamma - \gamma^*, \gamma - \gamma^*\right]\right|$$

$$\leqslant L\|\gamma - \gamma^*\|_{\infty,\Omega} |\gamma - \gamma^*|_{s,\Omega}^2.$$

Finally, a second order sufficient optimality condition is presented and proved.

Theorem 21. *Let $s \geqslant \frac{N}{q^*}$ and $\gamma^* \in \mathcal{A}$ such that γ^* verifies the first order optimality condition. If there exists $\delta > 0$ such that*

$$(\forall \gamma \in \mathcal{A}) J'' \left(\gamma^*\right) \left[\gamma - \gamma^*, \gamma - \gamma^*\right] \geqslant \delta \|\gamma - \gamma^*\|_{s,\Omega}^2.$$

Then, there exist $\sigma, \varepsilon > 0$, independent of γ and γ^*, such that

$$(\forall \gamma \in \mathcal{A}) \quad \|\gamma - \gamma^*\|_{\infty,\Omega} \leqslant \varepsilon \Rightarrow J (\gamma) \geqslant J \left(\gamma^*\right) + \sigma \|\gamma - \gamma^*\|_{s,\Omega}^2.$$

In consequence, J has a local minimum at γ^*.

Proof.   Applying a Taylor expansion, there exists $\theta \in (0, 1)$ such that

$$J\left(\gamma\right) = J\left(\gamma^*\right) + J'\left(\gamma^*\right)\left[\gamma - \gamma^*\right] + \frac{1}{2}J''\left(\theta\gamma^* + (1-\theta)\gamma\right)\left[\gamma - \gamma^*, \gamma - \gamma^*\right].$$

Using corollary 20, if $\varepsilon \leqslant \frac{\delta}{2L}$, $\sigma = \frac{\delta}{4}$ and $\|\gamma - \gamma^*\|_{\infty,\Omega} \leqslant \varepsilon$, then

$$J\left(\gamma\right) = J\left(\gamma^*\right) + J'\left(\gamma^*\right)\left[\gamma - \gamma^*\right] + \frac{1}{2}J''\left(\theta\gamma^* + (1-\theta)\gamma\right)\left[\gamma - \gamma^*, \gamma - \gamma^*\right]$$

$$\geqslant J\left(\gamma^*\right) + \frac{1}{2}J''\left(\theta\gamma^* + (1-\theta)\gamma\right)\left[\gamma - \gamma^*, \gamma - \gamma^*\right]$$

$$\geqslant J\left(\gamma^*\right) + \frac{1}{2}\left(J''\left(\theta\gamma^* + (1-\theta)\gamma\right) - J''\left(\gamma^*\right)\right)\left[\gamma - \gamma^*, \gamma - \gamma^*\right]$$

$$\quad + \frac{1}{2}J''\left(\gamma^*\right)\left[\gamma - \gamma^*, \gamma - \gamma^*\right]$$

$$\geqslant J\left(\gamma^*\right) + \frac{\delta}{2}\|\gamma - \gamma^*\|_{s,\Omega}^2 - \frac{L}{2}\|\gamma - \gamma^*\|_{\infty,\Omega}\|\gamma - \gamma^*\|_{s,\Omega}^2$$

$$\geqslant J\left(\gamma^*\right) + \frac{\delta}{2}\|\gamma - \gamma^*\|_{s,\Omega}^2 - \frac{\delta}{4}\|\gamma - \gamma^*\|_{s,\Omega}^2 = J\left(\gamma^*\right) + \sigma\|\gamma - \gamma^*\|_{s,\Omega}^2,$$

proving the theorem. □

Remark 22.   The result obtained in theorem 21 is conditioned to $s \geqslant \frac{N}{q^*}$. Considering the most pessimistic case, when $q^* = 2$, it is possible to establish that the simplest spaces for γ^*, where theorem 21 is valid, are $H^1\left(\Omega\right)$ and $H^2\left(\Omega\right)$ when $N = 2$ and $N = 3$, respectively.

6. Numerical results

In this section, the previous analysis is complemented by numerical experiments for the new parameter identification problem. Realistic synthetic cases are analyzed in 2D, which represent a longitudinal section of the structure of a cardiac valve in an arbitrary position. However, the numerical results presented below were obtained using the Navier–Stokes equation. So, the numerical problem to be solved is given by
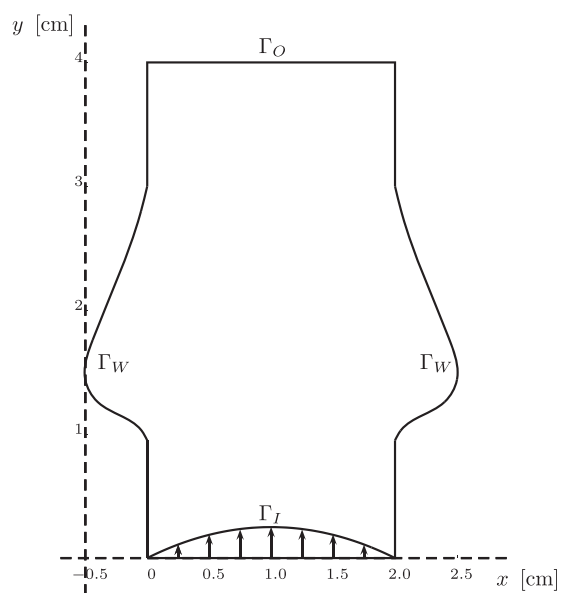
$$\text{minimize} \quad J\left(\gamma, \boldsymbol{u}\right) = \frac{1}{2}\|\boldsymbol{u} - \boldsymbol{u}_{\text{R}}\|_{0,\omega}^2 + \frac{\alpha}{2}\|\gamma\|_{1,\Omega}^2 \tag{8}$$

$$\begin{aligned}
\text{subject to} \quad -\nu\triangle\boldsymbol{u} + (\nabla\boldsymbol{u})\boldsymbol{u} + \nabla p + \gamma\boldsymbol{u} &= \boldsymbol{0} && \text{in } \Omega \\
\text{div } \boldsymbol{u} &= 0 && \text{in } \Omega \\
\boldsymbol{u} &= \boldsymbol{u}_{\text{D}} && \text{on } \Gamma_{\text{D}} \\
-\nu\frac{\partial\boldsymbol{u}}{\partial\boldsymbol{n}} + p\boldsymbol{n} &= \boldsymbol{0} && \text{on } \Gamma_N
\end{aligned} \tag{9}$$

$$\boldsymbol{u} \in \boldsymbol{H}^1\left(\Omega\right), \gamma \in H^1\left(\Omega\right)$$

$$0 \leqslant \gamma \leqslant M \quad \text{a.e. in } \Omega.$$

This special formulation of (9) is similar to (2) in terms of the resistance term. In the following subsections, the configurations of the reference case is explained, as well as the numerical

Figure 1. Domain for the numerical tests.
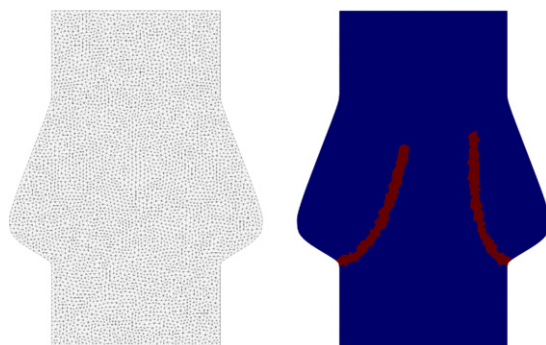
**Figure 2.** Plots of unstructured mesh (left) and γ (right).

solutions of the inverse problems associated with MRI images or Doppler ultrasound. Due to our lack of real images, our experiments are fully synthetic (figures 1–3).

6.1. Reference test

First, a reference geometry is defined. This geometry Ω represents the area around the aortic valve. The inflow Γ_I has a parabolic profile following Poiseuille's law given by

$$\boldsymbol{u}_D(x, y) = -Ux(d - x)\boldsymbol{n},$$

where $\boldsymbol{x} = (x, y)$ are the Cartesian coordinates of the domain, $\boldsymbol{n}$ is the outer normal vector and d is the diameter of the inflow, while do-nothing conditions are imposed on the outflow Γ_O
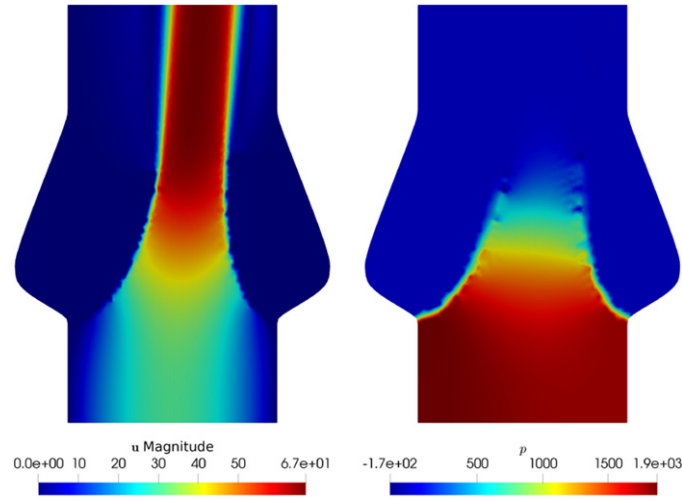
Figure 3. Reference solutions $\boldsymbol{u}$ and p.

given by

$$-\nu\frac{\partial \boldsymbol{u}}{\partial \boldsymbol{n}} + p\boldsymbol{n} = \boldsymbol{0}.$$

In the walls of the structure, represented by Γ_W, the fluid has no-slip conditions given by $\boldsymbol{u} = \boldsymbol{0}$.

The valves are modeled on the resistance term $\gamma\boldsymbol{u}$ using the function γ. This function assumes a constant value $M \gg 1$ in the regions where the valve is and assumes the value 0 where the valve is not. In order to define γ, a parabolic figure is drawn on each side Ω with an approximate thickness of 1 mm. When the valves are fully closed, they are symmetrical with respect to the vertical axis of symmetry. When the valves are open, these parabolas are rotated with respect to a reference system whose origin is at the point where the valve coincides with the walls of the structure given by Γ_W. Since blood flow is modeled, the kinematic viscosity is considered equal to $\nu = 0.035$ cm^2 s^{-1}, the density is assumed as $\rho = 1$ g cm^{-3}, and the dimensions $d = 2$ cm and $U = 30$ cm s^{-1}, resulting in a peak Reynolds number on the inlet of

$$\text{Re} = \frac{Ud}{\nu} = 1714.$$

The Navier–Stokes equations are discretized using the finite element method (FEM) with Taylor–Hood elements ($\mathbb{P}_2$ for the velocity $\boldsymbol{u}$ and $\mathbb{P}_1$ for the pressure) on an unstructured triangular mesh. The mesh used was generated by domain triangulation with $h = 0.05$ cm, which corresponds to 9950 elements and 4976 nodes. The solver is implemented using the finite element library FEniCS [2] with the default configuration. To solve the nonlinear problems, a Newton's method was used. The resistance γ is defined as a discontinuous function with discrete values in each element, assuming the value of $M = 10^8$ if the element intersects the valve or, otherwise, assumes the value 0. We define the set $\mathcal{O}$, that represents the valve inside of Ω, by

$$\mathcal{O} = \left\{ \boldsymbol{x} \in \Omega | \gamma(\boldsymbol{x}) = 10^8 \right\}.$$

6.2. Numerical solution of the inverse problem

Using the solution of the reference test as reference solution $\boldsymbol{u}_{\mathrm{R}}$, the following version of the model problem is solved numerically using FEniCS and Dolfin-adjoint

$$\text{minimize} \quad J(\gamma, \boldsymbol{u}) = \frac{1}{2}\|\boldsymbol{u} - \boldsymbol{u}_{\mathrm{R}}\|_{0,\omega}^2 + \frac{\alpha}{2}\|\gamma\|_{0,\Omega}^2 + \frac{\beta}{2}|\gamma|_{1,\Omega}^2 \tag{10}$$

$$\begin{aligned}
\text{subject to} \quad -\nu \triangle \boldsymbol{u} + (\nabla\boldsymbol{u})\boldsymbol{u} + \nabla p + \gamma\boldsymbol{u} &= \boldsymbol{0} && \text{in } \Omega \\
\text{div } \boldsymbol{u} &= 0 && \text{in } \Omega \\
\boldsymbol{u} &= \boldsymbol{u}_{\mathrm{D}} && \text{on } \Gamma_{\mathrm{I}} \\
\boldsymbol{u} &= \boldsymbol{0} && \text{on } \Gamma_{\mathrm{W}} \\
-\nu\frac{\partial\boldsymbol{u}}{\partial\boldsymbol{n}} + p\boldsymbol{n} &= \boldsymbol{0} && \text{on } \Gamma_N
\end{aligned} \tag{11}$$

$$\boldsymbol{u} \in \boldsymbol{H}^1(\Omega), \gamma \in H^1(\Omega)$$

$$0 \leqslant \gamma \leqslant C \quad \text{a.e. in } \Omega.$$

For this example, we considered a measurement area $\omega = \Omega$ and the values $C = 10^3$, $\alpha = 10^{-4}$ and $\beta = 10^{-8}$. The use of two different weights for the norm and seminorm is consistent with the theoretical analysis of the previous sections, so this problem has a solution. The dolfin-adjoint library [28] allows to implement automatic derivation of the discrete adjoint equations for pde models and implement minimization algorithms from the Python 3 libraries. In particular, the L-BFGS-B algorithm (see section 4.3 in [17]) was used with the following stopping criteria on the step k

$$\frac{|J(\gamma_k) - J(\gamma_{k+1})|}{\max\left\{|J(\gamma_k)|, |J(\gamma_{k+1})|, 1\right\}} \leqslant 10^{-6} \text{ or } \max_{j\in\{1 \dots n\}}\left\{|(\nabla J_k)_j|\right\} \leqslant 10^{-6},$$

where $(\nabla J_k)_j$ is the jth component of the projected gradient on the step k. To start the algorithm, $\gamma_0 = 0$ was used as the initial solution.

As a way to define a valve reconstruction algorithm sketch, we follow these steps.

(a) We defined an axis that crosses the domain from the inflow to the outflow.
(b) For a uniform discretization of the axis, we defined perpendicular lines.
(c) The solution γ^* obtained by the algorithm is interpolated on each of the lines. Three points are selected on each side of the axis. The first and second point are the limits of an interval where $\nabla\gamma^* \cdot \boldsymbol{n}$ has the maximum positive values with 1% of tolerance. The third point is the local maximum closest to the interval.
(d) An average is obtained between the three points.
(e) A polyline is drawn on each side of the axis. Each polyline passes through all the average points.

Numerical results are presented in figure 4. The polyline is drawn in white, which presents a great approximation to the interface between the different values of the reference given by γ.

The optimal γ^* has values close to 0 in the areas before and after the valves. On the other hand, in the interior area where there are no valves, the optimal solution takes values close to 0. Likewise, the magnitude and direction of $\boldsymbol{u}^*$ is similar to $\boldsymbol{u}_{\mathrm{R}}$, where $\boldsymbol{u}^*$ corresponds to the optimal state.
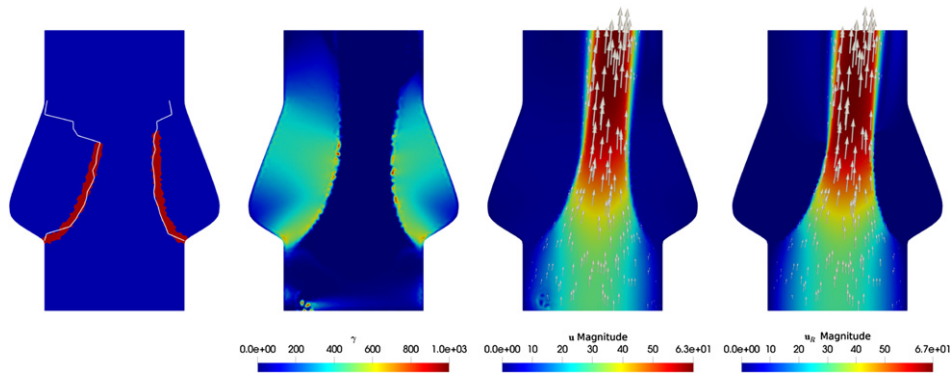
Figure 4. Real γ and reconstructed valve, optimal γ, optimal $\boldsymbol{u}$, and reference solution $\boldsymbol{u}_{\mathrm{R}}$ (from left to right). Reference test, 148 iterations.
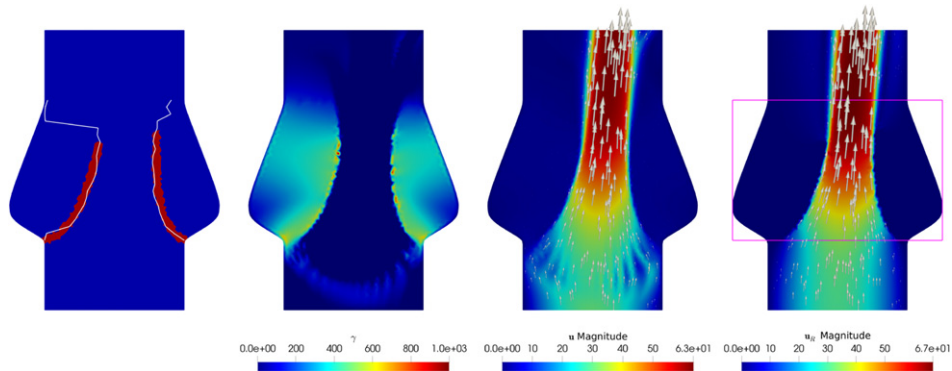
Figure 5. Real γ and reconstructed valve, optimal γ, optimal $\boldsymbol{u}$, and reference solution $\boldsymbol{u}_{\mathrm{R}}$ (from left to right). Reference test with subdomain, 240 iterations.

It is necessary to corroborate that this algorithm is able to solve the inverse problem measuring only a part of $\boldsymbol{u}_{\mathrm{R}}$ given by the reference velocity. In this case, choosing ω as the area where the valves should be (see figure 5 right), given by

$$\omega = \Omega \cap \left\{ (x, y) \in \mathbb{R}^2 | 1 \leqslant y \leqslant 3 \right\},$$

the expected result should be similar to that found above.

Figure 5 presents the numerical results, the polyline and the references. In the case of the reference solution $\boldsymbol{u}_{\mathrm{R}}$, a pink rectangle was drawn that allows delimiting the measurement area ω. In particular, this problem required more iterations than the case with measurements on Ω, obtaining very similar results.

6.3. Measurements of MRI type

Using the reference solutions, it is possible to generate synthetic measurements that represent the behavior of MRI velocity type measurements. A 2D plane is chosen on which the velocity is measured in one specified direction $\boldsymbol{d} \in \mathbb{R}^2$, with $|\boldsymbol{d}| = 1$. Then, the measurement is given by
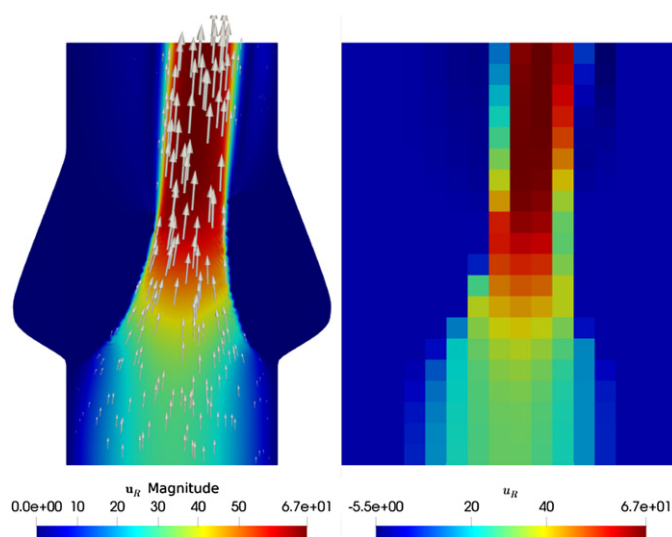
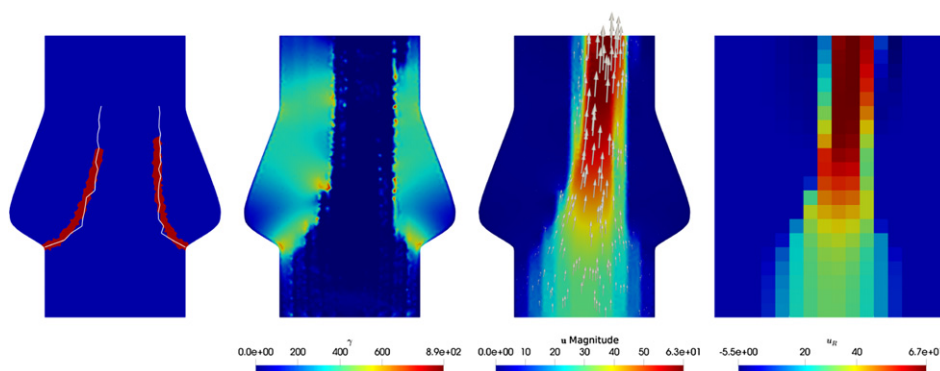**Figure 6.** Reference u_R (left) and synthetic MRI type velocity measurement (u_R, right).

Figure 7. Real γ and reconstructed valve, optimal γ, optimal $\boldsymbol{u}$, and synthetic MRI (from left to right). MRI noiseless.

$$u_R = \boldsymbol{u}_R \cdot \boldsymbol{d}.$$

The MRI type velocity measurement data is represented in a mesh of uniform quadrilaterals of 2 mm × 2 mm. They are obtained by projecting u_R to the $\mathbb{Q}_0$ finite element space, given by piecewise constant discontinuous functions on the quadrilateral mesh. In practical applications, the input speed is unknown and must be estimated. Then, a direction $\boldsymbol{d}$ for this MRI can be chosen as that which is an inner normal to Γ_I. To determine U, the projection of u_R in $L_2(\Gamma_I)$ with respect to $Ux(2 - x)$ is calculated by

$$U = \frac{\int_{\Gamma_I} u_R [x(2 - x)] \, dS}{\int_{\Gamma_I} [x(2 - x)]^2 \, dS}.$$

17

Thus, U approaches in a least squares sense. Figure 6 shows the synthetic MRI generated from the reference solution.

The new problem to solve is given by

$$\text{minimize} \quad J\left(\gamma, \boldsymbol{u}\right) = \frac{1}{2}\|(\boldsymbol{u} - \boldsymbol{u}_{\mathrm{R}}) \cdot \boldsymbol{d}\|_{0,\Omega}^2 + \frac{\alpha}{2}\|\gamma\|_{0,\Omega}^2 + \frac{\beta}{2}|\gamma|_{1,\Omega}^2 \tag{12}$$

$$
\begin{aligned}
\text{subject to} \quad -\nu \triangle \boldsymbol{u} + (\nabla \boldsymbol{u})\boldsymbol{u} + \nabla p + \gamma \boldsymbol{u} &= \boldsymbol{0} && \text{in } \Omega \\
\operatorname{div} \boldsymbol{u} &= 0 && \text{in } \Omega \\
\boldsymbol{u} &= \boldsymbol{u}_{\mathrm{D}} && \text{on } \Gamma_{\mathrm{I}} \\
\boldsymbol{u} &= \boldsymbol{0} && \text{on } \Gamma_{\mathrm{W}} \\
-\nu \frac{\partial \boldsymbol{u}}{\partial \boldsymbol{n}} + p\boldsymbol{n} &= \boldsymbol{0} && \text{on } \Gamma_N
\end{aligned}
\tag{13}
$$

$$\boldsymbol{u} \in \boldsymbol{H}^1\left(\Omega\right), \gamma \in H^1\left(\Omega\right)$$

$$0 \leqslant \gamma \leqslant \quad C \text{ a.e. in } \Omega,$$

where the values $C = 10^3$, $\alpha = 10^{-4}$ and $\beta = 10^{-8}$ were used. It is possible to prove the existence of solution of this problem in the same way as in the proof of the theorem. Figure 7 shows the numerical results and the references. The parameter γ has some jumps that coincide with the vertical lines between the MRI voxels, while the polyline tends to have segments parallel to those vertical lines, but it acceptably approximates the space between the valves.

The white noise intensity in the velocity measurements from MRI is proportional to the velocity encoding parameter (also called VENC [18]) of the scan. This parameter is configured with a value greater than the maximum expected velocity, in order to eliminate signal aliasing. Then, the noise in all voxels is proportional to the maximum velocity in the measurement area. In the clinical practice it can be expected that high-quality MRI contains a velocity noise of 10% of the maximum velocity in each voxel [18]. Gaussian noises were added to this MRI with a standard deviation of 5%, 10% and 20% of the maximum value of u_{R}.

Figure 8 shows the results of this experiment with a 5% of Gaussian noise, but changing the weights to $\alpha = 10^{-4}$ and $\beta = 10^{-6}$ in terms to decrease the effects of noise. The results are similar to the experiment without noise in terms to the tendency of the polyline to approximate the valve shape and draw lines parallel to the voxels.

This approximation seems weaker as noise increases, in the sense that the polyline has a lower quality in its approximation and that the gamma function tends to overfit the data. The following two figures show the result of the experiment with 10% and 20% of Gaussian noise, respectively. The noise is exactly the same than the 5% Gaussian noise case, but increasing the level noise.

Table 1 shows the mean square error (MSE) between the reconstructed valve given by the polylines obtained using MRI in figures 7–10, and the polyline obtained in the reference test (see figure 4). To quantify this error, we consider only the points of the polyline in figure 4 that are at a distance less than or equal to 0.5 mm from $\mathcal{O}$. There are minor differences between the valve reconstructions for the cases with a noise level of 5% and 10%. However, the quality of the reconstruction decreases when the level noise increases up to 20%.

Figure 11 shows the reconstructed polyline for three experiments with independent noises at same level of noise. Each polyline color represents the final result of this experiment with
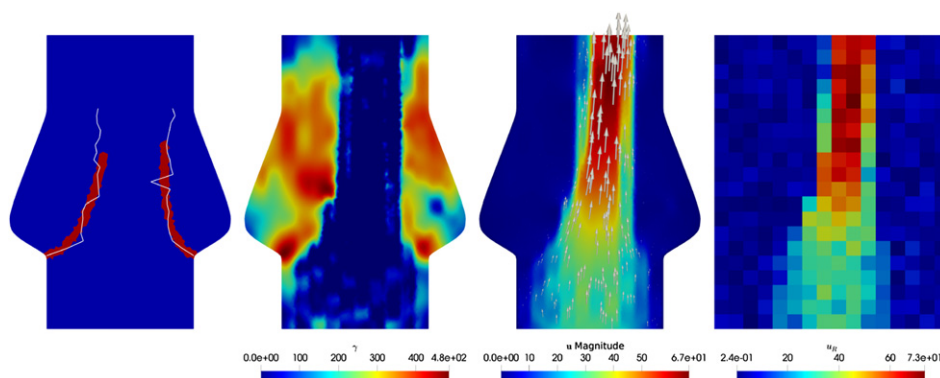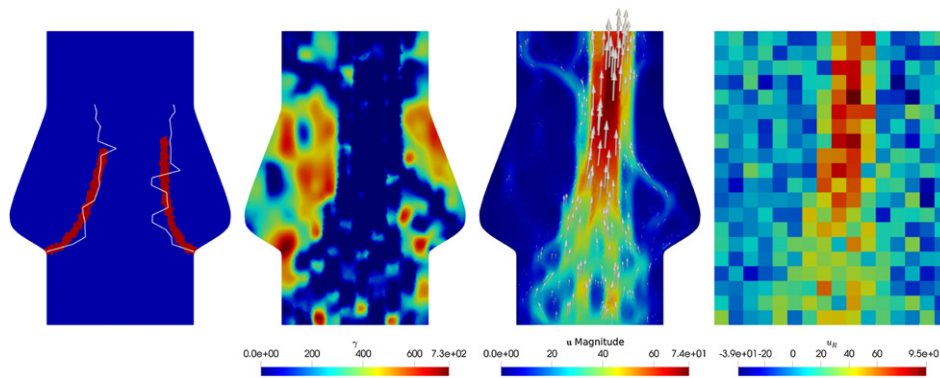
Figure 8. Real γ and reconstructed valve, optimal γ, optimal $\boldsymbol{u}$, and synthetic MRI (from left to right). MRI with 5% of noise.

Table 1. MSE of reconstructed valves using MRI with different noise levels.

Noise level	MSE
0%	4.4680×10^{-3}
5%	8.6308×10^{-3}
10%	8.1992×10^{-3}
20%	1.5016×10^{-2}
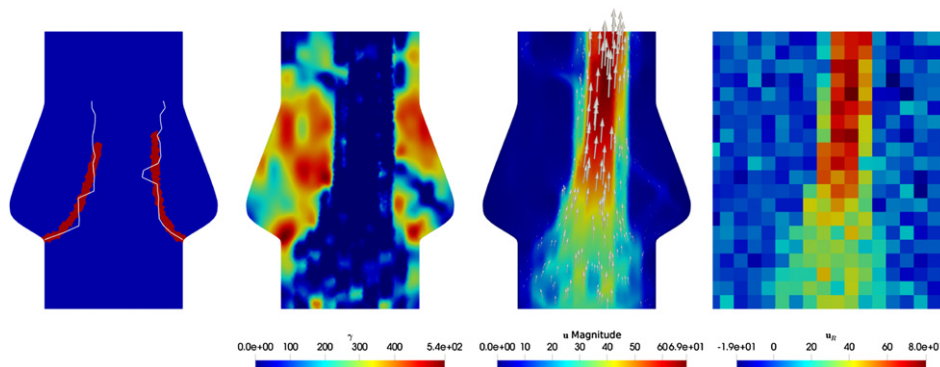
Figure 9. Real γ and reconstructed valve, optimal γ, optimal $\boldsymbol{u}$, and synthetic MRI (from left to right). MRI with 10% of noise.

a Gaussian noise independent of the others, whose amplitude was adjusted for the noise level of 5%, 10% and 20%. We can see that the rebuilt valves are more irregular as the noise level increases, especially for 20% of level noise, which is consistent with table 1.

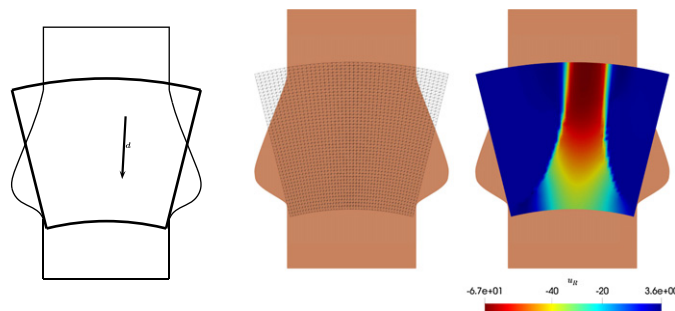### 6.4. Measurements of ultrasound imaging type

It is possible to generate synthetic measurements similar to ultrasound images. From a given focal point, directional velocities are measured at each point in a domain with the form of

Figure 10. Real γ and reconstructed valve, optimal γ, optimal $\boldsymbol{u}$, and synthetic MRI (from left to right). MRI with 20% of noise.
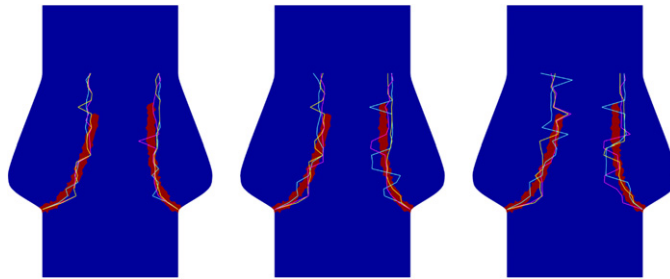

Figure 11. Comparison of reconstructed valves with three different noises, with 5%, 10% and 20% of noise (from left to right).

Figure 12. Ultrasound imaging domain, mesh and synthetic ultrasound imaging.

a circular sector with center in the focal point. The chosen directions $\boldsymbol{d}(\boldsymbol{x})$ are given by unit vectors parallel to the vector that joins the measurement point with the focal point. Then, the measurement is given by

$$u_{\mathrm{R}} = \boldsymbol{u}_{\mathrm{R}} \cdot \boldsymbol{d}(x).$$
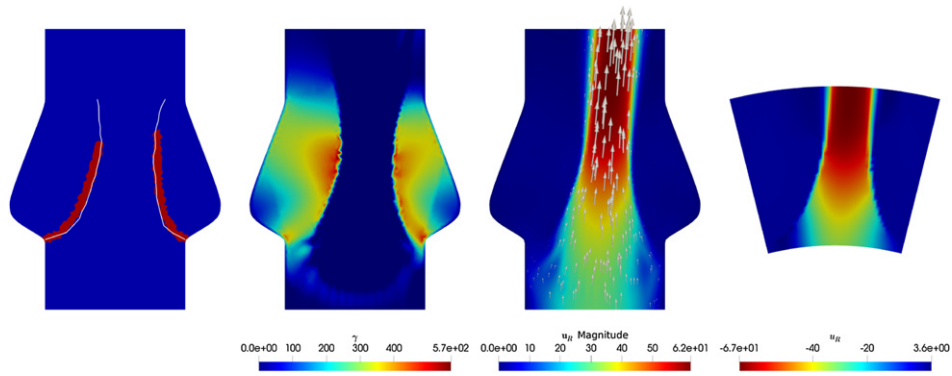
Figure 13. Real γ and reconstructed valve, optimal γ, optimal $\boldsymbol{u}$, and synthetic ultrasound imaging(from left to right).

The measurement data is represented in a structured triangular mesh of 2116 nodes and 4050 triangles with $h = 0.067$ cm. The measurements are obtained by interpolation of u_R to the $\mathbb{P}_1$ finite element space defined on the structured mesh (figure 12). Again, the input speed is unknown and must be estimated from a preliminary measurement. To determine U, the projection of u_R in $L_2\left(\Gamma_\mathrm{I}\right)$ with respect to $Ux(2 - x)\left[\boldsymbol{n} \cdot \boldsymbol{d}\left(x\right)\right]$ is calculated by

$$U = \frac{\int_{\Gamma_\mathrm{I}} u_\mathrm{R}\left[x\left(2 - x\right)\right]\left[\boldsymbol{n} \cdot \boldsymbol{d}\left(\boldsymbol{x}\right)\right]\mathrm{d}S}{\int_{\Gamma_\mathrm{I}}\left[x\left(2 - x\right)\right]^2\left[\boldsymbol{n} \cdot \boldsymbol{d}\left(\boldsymbol{x}\right)\right]^2\,\mathrm{d}S}.$$

The new problem to solve is given by

$$\text{minimize} \quad J\left(\gamma, \boldsymbol{u}\right) = \frac{1}{2}\left\|\left(\boldsymbol{u} - \boldsymbol{u}_\mathrm{R}\right) \cdot \boldsymbol{d}\left(\boldsymbol{x}\right)\right\|_{0,\omega}^2 + \frac{\alpha}{2}\left\|\gamma\right\|_{0,\Omega}^2 + \frac{\beta}{2}\left|\gamma\right|_{1,\Omega}^2 \tag{14}$$

$$
\begin{aligned}
\text{subject to} \quad & -\nu \triangle \boldsymbol{u} + \left(\nabla\boldsymbol{u}\right)\boldsymbol{u} + \nabla p + \gamma\boldsymbol{u} = \boldsymbol{0} && \text{in } \Omega \\
& \operatorname{div}\boldsymbol{u} = 0 && \text{in } \Omega \\
& \boldsymbol{u} = \boldsymbol{u}_\mathrm{D} && \text{on } \Gamma_\mathrm{I} \\
& \boldsymbol{u} = \boldsymbol{0} && \text{on } \Gamma_\mathrm{W} \\
& -\nu\frac{\partial\boldsymbol{u}}{\partial\boldsymbol{n}} + p\boldsymbol{n} = \boldsymbol{0} && \text{on } \Gamma_N
\end{aligned}
\tag{15}
$$

$$\boldsymbol{u} \in \boldsymbol{H}^1\left(\Omega\right), \gamma \in H^1\left(\Omega\right)$$

$$0 \leqslant \gamma \leqslant C \text{ a.e. in } \Omega$$

where ω is the subdomain on Ω covered by the ultrasound imaging and the values $C = 10^3$, $\alpha = 10^{-4}$ and $\beta = 10^{-8}$ were used. This problem has solution, and the proof of the existence of solution is similar to the proof of the theorem. Figure 13 presents the numerical results, the polyline and the references. The results obtained are very similar to those obtained in the reference tests with measurements in the entire domain and in a subdomain.

There are multiple sources of noise in ultrasound images, such as reverberation, ghosting, or fake echo, among others. Therefore, it is not possible to define a simplified structure of noise in this type of images [9, 25]. In order to study the effect of the noise, we assume an additive
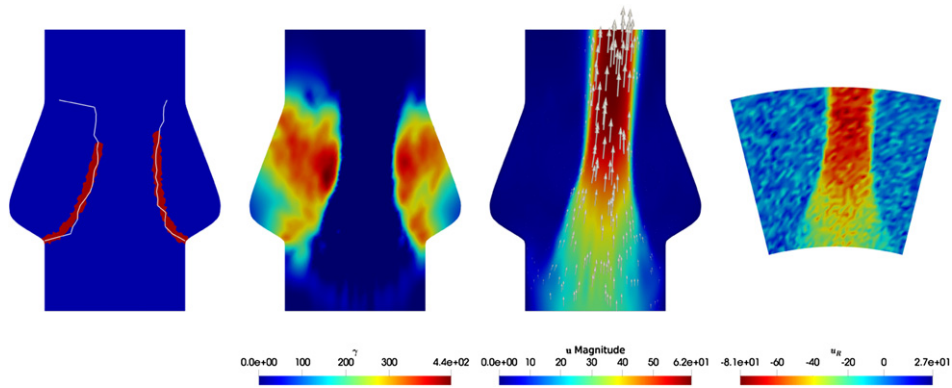
Figure 14. Real γ and reconstructed valve, optimal γ, optimal $\boldsymbol{u}$, and synthetic ultrasound imaging (from left to right) with 10% of noise.
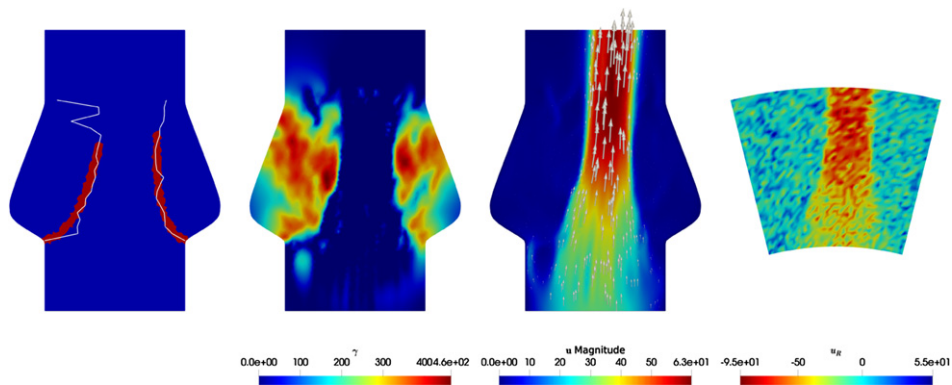
Figure 15. Real γ and reconstructed valve, optimal γ, optimal $\boldsymbol{u}$, and synthetic ultrasound imaging (from left to right) with 20% of noise.

Gaussian noise that is proportional to the maximum of $|u_R|$ in the measurement area. From [24], an experiment with a straight-vessel phantom had a 9.6% of standard deviation. Then, is acceptable to simulate an ultrasound imaging with a velocity noise of 10% of the maximum velocity in each node. Gaussian noises were added to this ultrasound imaging with a standard deviation of 10% and 20% of the maximum of $|u_R|$.

Figures 14 and 15 show the results of this experiment with a 10% and 20% of Gaussian noise, respectively, but changing the weights to $\alpha = 10^{-4}$ and $\beta = 10^{-6}$ in terms to decrease the effects of noise. The results are similar to the experiment without noise in terms to the tendency of the polyline to approximate the valve shape.

Table 2 shows the MSE between the reconstructed valve given by the polylines obtained using MRI in figures 13–15, and the polyline obtained in the reference test with measurement in a subdomain (see figure 5). The MSE was quantified by the same way as in table 1. There are minor differences between the valve reconstructions for the cases with a noise level of 10% and 20%.

Table 2. MSE of reconstructed valves using ultrasound imaging with different noise levels.

Noise level	MSE
0%	3.0985×10^{-3}
10%	8.1993×10^{-3}
20%	8.6772×10^{-3}

7. Conclusions

We have presented a new parameter identification problem for the Oseen equation, contributing to the detection of obstacles in fluid dynamic studies. For this problem, the existence of solution and optimality conditions were determined. The study of optimality conditions is necessary to validate the use of optimization algorithms. In particular, the second order optimality condition allowed to specify the H^s space where the parameter γ belongs.

The numerical experiments developed in this work allow us to conjecture that it would be possible to extend this analysis for the Navier–Stokes equation. Indeed, the numerical tests without noise had satisfactory results in terms of rebuilding the simulated valve. Furthermore, experiments with Gaussian noise show that disturbances in the reference image are reflected in bounded changes in the parameter and in the reconstructed valve. The quality of the solutions is worse as noise increases, as expected.

There are several ways to deepen this work. From an analytical perspective, it is necessary to repeat the theoretical analysis for problem (9), in the same way as we worked with problem (1), looking for obtaining similar results. Future work will tackle the uniqueness and stability of the solution of this new inverse problem. Related works on obstacle estimation via shape optimization in the Brinkman problem [29] or source estimation in the Brinkman [26] and transient Navier–Stokes equations [15] could serve as a starting point.

Based on the favorable numerical results, the next step is to perform experiments with 3D domains, including structures and real images (both MRI and ultrasound imaging), whether obtained from phantoms or real patients. The 3D case is of medical interest, since it will contribute to simplify the detection of defects in the function of aortic valves, among other structures. Therefore, designing an algorithm to recreate the aortic valve in 3D is also one of the future improvements.

Acknowledgments

Appendix A. Proof of theorem 7

Theorem. *A is Fréchet-differentiable. For each $\gamma, \gamma_1 \in \mathcal{A}$, if $A(\gamma) = [\boldsymbol{v}, p]$, then the Fréchet derivative $A'(\gamma)[\gamma_1] = [\boldsymbol{v}'_1, p'_1]$ can be described by the weak solution of the following problem*

$$-\nu \triangle \boldsymbol{v}_1' + \left(\nabla \boldsymbol{v}_1'\right)\boldsymbol{a} + \nabla p_1' + \gamma \boldsymbol{v}_1' = -\gamma_1 \left(\boldsymbol{v} + \boldsymbol{G}\right) \qquad in\ \Omega$$

$$\mathrm{div}\ \boldsymbol{v}_1' = 0 \qquad in\ \Omega$$

$$\boldsymbol{v}_1' = \boldsymbol{0} \qquad on\ \Gamma_{\mathrm{D}}$$

$$-\nu \frac{\partial \boldsymbol{v}_1'}{\partial \boldsymbol{n}} + p_1' \boldsymbol{n} = \boldsymbol{0} \qquad on\ \Gamma_N.$$

Proof. Let $\gamma, \gamma_1 \in \mathcal{A}$, it will be proved that there is a linear application $D : L^\infty(\Omega) \to \mathcal{H}$ such that

$$A\left(\gamma + \gamma_1\right) - A\left(\gamma\right) = D\left(\gamma_1\right) + r\left(\gamma, \gamma_1\right),$$

where

$$\|\gamma_1\|_{\infty,\Omega} \to 0 \Rightarrow \frac{\|r\left(\gamma,\gamma_1\right)\|_{\mathcal{H}}}{\|\gamma_1\|_{\infty,\Omega}} \to 0.$$

Let $[\boldsymbol{v}_1, p_1] = A\left(\gamma + \gamma_1\right)$. Taking $D\left(\gamma_1\right) = \left[\boldsymbol{v}_1', p_1'\right]$ and $r\left(\gamma, \gamma_1\right) = [\delta \boldsymbol{v}, \delta p] = \left[\boldsymbol{v}_1 - \boldsymbol{v} - \boldsymbol{v}_1', p_1 - p - p_1'\right]$, it is possible to see that $D\left(\gamma_1\right)$ is linear. Also, $r\left(\gamma, \gamma_1\right)$ is solution of the problem

$$-\nu \triangle \left(\delta \boldsymbol{v}\right) + \left(\nabla \delta \boldsymbol{v}_1\right)\boldsymbol{a} + \nabla\left(\delta p\right) + \gamma\left(\delta \boldsymbol{v}\right) = \gamma_1 \left(v - v_1\right) \qquad in\ \Omega$$

$$\mathrm{div}\left(\delta \boldsymbol{v}\right) = 0 \qquad in\ \Omega$$

$$\left(\delta \boldsymbol{v}\right) = \boldsymbol{0} \qquad on\ \Gamma_{\mathrm{D}}$$

$$-\nu \frac{\partial\left(\delta \boldsymbol{v}\right)}{\partial \boldsymbol{n}} + \left(\delta p\right)\boldsymbol{n} = \boldsymbol{0} \qquad on\ \Gamma_N.$$

Thus, there exists a constant $c_1 > 0$, independent of γ and γ_1 (see lemma 5.8 on [23]), such that

$$\|r\left(\gamma,\gamma_1\right)\|_{\mathcal{H}} = \nu|\delta \boldsymbol{v}|_{1,\Omega} + \|\delta p\|_{0,\Omega} \leqslant c_1 \|\gamma_1\|_{0,\Omega}\|\boldsymbol{v} - \boldsymbol{v}_1\|_{0,\Omega}.$$

subtracting the equations of $\boldsymbol{v}$ y $\boldsymbol{v}_1$ and using integration by parts,

$$\nu|\boldsymbol{v} - \boldsymbol{v}_1|_{1,\Omega}^2 + \left(\gamma\left(\boldsymbol{v} - \boldsymbol{v}_1\right), \boldsymbol{v} - \boldsymbol{v}_1\right)_{0,\Omega} = \left(\gamma_1\left(\boldsymbol{G} + \boldsymbol{v}_1\right), \boldsymbol{v} - \boldsymbol{v}_1\right)_{0,\Omega}.$$

Applying Cauchy–Schwarz and Friedrichs–Poincaré inequalities, there exists $c_2 > 0$ such that

$$\nu|\boldsymbol{v} - \boldsymbol{v}_1|_{1,\Omega}^2 \leqslant \left(\gamma_1\left(\boldsymbol{G} + \boldsymbol{v}_1\right), \boldsymbol{v} - \boldsymbol{v}_1\right)_{0,\Omega}$$

$$\leqslant \|\gamma_1\|_{\infty,\Omega}\|\boldsymbol{G} + \boldsymbol{v}_1\|_{0,\Omega}\|\boldsymbol{v} - \boldsymbol{v}_1\|_{0,\Omega}$$

$$\leqslant c_2\|\gamma_1\|_{\infty,\Omega}\|\boldsymbol{G} + \boldsymbol{v}_1\|_{0,\Omega}|\boldsymbol{v} - \boldsymbol{v}_1|_{1,\Omega}.$$

But, using Friedrichs–Poincaré inequality again, there exists $c_3 > 0$ such that $\|\boldsymbol{G} + \boldsymbol{v}_1\|_{0,\Omega} \leqslant c_3\|\boldsymbol{G}\|_{1,\Omega}$ (see remark 5). Then, there exists $C_1 > 0$ such that

$$\nu|\boldsymbol{v} - \boldsymbol{v}_1|_{1,\Omega} \leqslant C_1\|\gamma_1\|_{\infty,\Omega}\|\boldsymbol{G}\|_{0,\Omega}.$$

Finally, applying Friedrichs–Poincaré inequality, there exists a constant $C > 0$ such that

$$\|r\left(\gamma,\gamma_1\right)\|_{\mathcal{H}} = \nu|\delta \boldsymbol{v}|_{1,\Omega} + \|\delta p\|_{0,\Omega} \leqslant C\|\gamma_1\|_{\infty,\Omega}^2 \|\boldsymbol{G}\|_{0,\Omega}.$$

Thus,

$$\frac{\|r(\gamma, \gamma_1)\|_{\mathcal{H}}}{\|\gamma_1\|_{\infty,\Omega}} \leqslant C\|\gamma_1\|_{0,\Omega}\|\boldsymbol{G}\|_{0,\Omega} \overset{\|\gamma_1\|_{\infty,\Omega}\to 0}{\rightarrow} 0,$$

proving the theorem.   □

Appendix B. Proof of theorem 14

Theorem. *The map $\gamma \longmapsto A'(\gamma)[\gamma_1]$ from $L^\infty(\Omega)$ to $\mathcal{H}$ for each $\gamma_1 \in \mathcal{A}$ is Fréchet-differentiable. Let $\gamma, \gamma_1, \gamma_2 \in\in \mathcal{A}$, the Fréchet derivative of $A'(\gamma)[\gamma_1]$ on γ_2 direction is given by $A''(\gamma)[\gamma_1, \gamma_2] = [\boldsymbol{v}'', p'']$, where $[\boldsymbol{v}'', p'']$ is the unique weak solution of the problem*

$$\begin{aligned}
-\nu \triangle \boldsymbol{v}'' + (\nabla\boldsymbol{v}'')\,\boldsymbol{a} + \nabla p'' + \gamma\boldsymbol{v}'' &= -(\gamma_2\boldsymbol{v}'_1 + \gamma_1\boldsymbol{v}'_2) && \text{in } \Omega \\
\text{div } \boldsymbol{v}'' &= 0 && \text{in } \Omega \\
\boldsymbol{v}'' &= \boldsymbol{0} && \text{on } \Gamma_D \\
-\nu\frac{\partial\boldsymbol{v}''}{\partial\boldsymbol{n}} + p''\boldsymbol{n} &= \boldsymbol{0} && \text{on } \Gamma_N.
\end{aligned} \tag{B.1}$$

and $A'(\gamma)\gamma_j = [\boldsymbol{v}'_j, p'_j]$, for $j \in \{1, 2\}$.

Proof. Let $\gamma, \gamma_1 \in \mathcal{A}$, it will be proved that there is a linear application $D_2 : L^\infty(\Omega) \to \mathcal{H}$ such that

$$A'(\gamma + \gamma_2)[\gamma_1] - A'(\gamma)[\gamma_1] = D_2(\gamma, \gamma_1)[\gamma_2] + r(\gamma, \gamma_1, \gamma_2),$$

where

$$\|\gamma_2\|_{\infty,\Omega} \to 0 \Rightarrow \frac{\|r(\gamma, \gamma_1, \gamma_2)\|_{\mathcal{H}}}{\|\gamma_2\|_{\infty,\Omega}} \to 0.$$

Let $A'(\gamma + \gamma_2)[\gamma_1] = [\boldsymbol{w}'_1, q'_1]$, $A'(\gamma)[\gamma_1] = [\boldsymbol{v}'_1, p'_1]$ (see theorem 7), $A(\gamma) = [\boldsymbol{v}, p]$ and $A(\gamma + \gamma_2) = [\boldsymbol{w}, q]$ (see definition 4). Defining $D(\gamma, \gamma_1)[\gamma_2] = [\boldsymbol{v}'', p'']$ as function of γ_2 and

$$r(\gamma, \gamma_1, \gamma_2) = [\delta\boldsymbol{v}, \delta p] = [\boldsymbol{w}'_1 - \boldsymbol{v}'_1 - \boldsymbol{v}'', q'_1 - p'_1 - p''],$$

it is possible to see that $D(\gamma, \gamma_1)$ is linear and $r(\gamma, \gamma_1, \gamma_2)$ is solution of the problem

$$\begin{aligned}
-\nu \triangle(\delta\boldsymbol{v}) + (\nabla\delta\boldsymbol{v})\boldsymbol{a} + \nabla(\delta p) + \gamma(\delta\boldsymbol{v}) &= \gamma_2\left(\boldsymbol{v}'_1 - \boldsymbol{w}'_1\right) + \gamma_1\left(\boldsymbol{v}'_2 + \boldsymbol{v} - \boldsymbol{w}\right) && \text{in } \Omega \\
\text{div}(\delta\boldsymbol{v}) &= 0 && \text{in } \Omega \\
(\delta\boldsymbol{v}) &= \boldsymbol{0} && \text{on } \Gamma_D \\
-\nu\frac{\partial(\delta\boldsymbol{v})}{\partial\boldsymbol{n}} + (\delta p)\boldsymbol{n} &= \boldsymbol{0} && \text{on } \Gamma_N.
\end{aligned}$$

Then, applying Friedrichs–Poincaré inequality, there exists $c_1 > 0$, independent of $\gamma, \gamma_1, \gamma_2$ such that

$$\nu|\delta\boldsymbol{v}|_{1,\Omega} + \|\delta p\|_{0,\Omega} \leqslant c_1\left(\|\gamma_2\|_{\infty,\Omega}|\boldsymbol{v}'_1 - \boldsymbol{w}'_1|_{1,\Omega} + \|\gamma_1\|_{\infty,\Omega}|\boldsymbol{v}'_2 + \boldsymbol{v} - \boldsymbol{w}|_{1,\Omega}\right).$$

Later, subtracting the equations of v'_1 and w'_1, testing with $v'_1 - w'_1$ and $p'_1 - q_1$, respectively, and applying Friedrichs–Poincaré inequality, there exists $c_2 > 0$ such that

$$\nu\left|v'_1 - w'_1\right|^2_{1,\Omega} \leqslant \left(\gamma_2 w'_1, v'_1 - w'_1\right)_{0,\Omega} + \left(\gamma_1\left(w - v\right), v'_1 - w'_1\right)_{0,\Omega}$$

$$\leqslant \|\gamma_2\|_{\infty,\Omega}\|w'_1\|_{0,\Omega}\|v'_1 - w'_1\|_{0,\Omega} + \|\gamma_1\|_{\infty,\Omega}\|w - v\|_{0,\Omega}\|v'_1 - w'_1\|_{0,\Omega}$$

$$\leqslant c_2\left(\|\gamma_2\|_{\infty,\Omega}|w'_1|_{1,\Omega} + \|\gamma_1\|_{\infty,\Omega}|w - v|_{1,\Omega}\right)|v'_1 - w'_1|_{1,\Omega}.$$

Hence,

$$\nu|v'_1 - w'_1|_{1,\Omega} \leqslant c_2\left(\|\gamma_2\|_{\infty,\Omega}|w'_1|_{1,\Omega} + \|\gamma_1\|_{\infty,\Omega}|w - v|_{1,\Omega}\right).$$

Analogously, from the equations of w and v, there exists $c_2 > 0$ such that

$$\nu|w - v|^2_{1,\Omega} \leqslant -\left(\gamma_2\left(v + G\right), w - v\right)_{0,\Omega}$$

$$\leqslant \|\gamma_2\|_{\infty,\Omega}\|v + G\|_{0,\Omega}\|w - v\|_{0,\Omega}$$

$$\leqslant c_2\|\gamma_2\|_{\infty,\Omega}|v + G|_{1,\Omega}|w - v|_{1,\Omega},$$

but there exists $c_3 > 0$ such that $|v|_{1,\Omega} \leqslant c_3\|G\|_{1,\Omega}$ (see remark 5). Then,

$$\nu|w - v|_{1,\Omega} \leqslant c_2 c_3\|\gamma_2\|_{\infty,\Omega}\|G\|_{1,\Omega}.$$

Futhermore, there exists $c_4 > 0$ such that

$$\nu|w'_1|_{1,\Omega} \leqslant c_4\|G\|_{1,\Omega}.$$

In conclusion, there exists $C_1 > 0$ such that

$$\nu|v'_1 - w'_1|_{1,\Omega} \leqslant C_1\|\gamma_1\|_{\infty,\Omega}\|\gamma_2\|_{\infty,\Omega}\|G\|_{1,\Omega}.$$

Repeating this analysis for the term $v'_2 + v - w$, there exists $c_5 > 0$ such that

$$\nu|v'_2 + v - w|_{0,\Omega} \leqslant c_5\|\gamma_2\|_{\infty,\Omega}|w - v|_{1,\Omega}$$

$$\leqslant c_5\|\gamma_2\|^2_{\infty,\Omega}\|G\|_{1,\Omega}.$$

Then, there exists $C_2 > 0$ such that

$$\|r\left(\gamma,\gamma_1,\gamma_2\right)\|_{\mathcal{H}} = \nu|\delta v|_{1,\Omega} + \|\delta p\|_{0,\Omega}$$

$$\leqslant c_1\left(\|\gamma_2\|_{\infty,\Omega}|v'_1 - w'_1|_{0,\Omega} + \|\gamma_1\|_{\infty,\Omega}|v'_2 + v - w|_{1,\Omega}\right)$$

$$\leqslant c_1\left(c_2\|\gamma_1\|_{\infty,\Omega}\|\gamma_2\|^2_{\infty,\Omega}\|G\|_{1,\Omega} + c_5 c_2\|\gamma_1\|_{\infty,\Omega}\|\gamma_2\|^2_{\infty,\Omega}\|G\|_{1,\Omega}\right)$$

$$\leqslant C_2\|\gamma_1\|_{\infty,\Omega}\|\gamma_2\|^2_{\infty,\Omega}\|G\|_{1,\Omega}.$$

In conclusion,

$$\frac{\|r\left(\gamma,\gamma_1,\gamma_2\right)\|_{\mathcal{H}}}{\|\gamma_2\|_{\infty,\Omega}} \leqslant C_2\|\gamma_1\|_{\infty,\Omega}\|\gamma_2\|_{\infty,\Omega}\|G\|_{0,\Omega} \overset{\|\gamma_2\|_{\infty,\Omega}\to 0}{\to} 0,$$

proving the theorem □

ORCID iDs

Jorge Aguayo ⓘ https://orcid.org/0000-0002-3644-280X

References

[1] Abraham F, Behr M and Heinkenschloss M 2004 The effect of stabilization in finite element methods for the optimal boundary control of the Oseen equations *Finite Elem. Anal. Des.* **41** 229–51

[2] Alnæs M *et al* 2015 The FEniCS project version 1.5 *Arch. Numer. Softw.* **3** 9–23

[3] Alvarez C, Conca C, Friz L, Kavian O and Ortega J H 2005 Identification of immersed obstacles via boundary measurements *Inverse Problems* **21** 1531

[4] Aßmann U and Rösch A 2013 Identification of an unknown parameter function in the main part of an elliptic partial differential equation *Z. Anal. Anwend.* **32** 163–72

[5] Astorino M, Hamers J, Shadden S C and Gerbeau J-F 2012 A robust and efficient valve model based on resistive immersed surfaces *Int. J. Numer. Methods Biomed. Eng.* **28** 937–59

[6] Auriault J-L 2008 On the domain of validity of Brinkman's equation *Transp. Porous Med.* **79** 215–23

[7] Ballerini A 2010 Stable determination of an immersed body in a stationary Stokes fluid *Inverse Problems* **26** 125015

[8] Bertoglio C *et al* 2017 Benchmark problems for numerical treatment of backflow at open boundaries *Int J. Numer. Methods Biomed Eng.* **34** e2918

[9] Bjærum S, Torp H and Kristoffersen K 2002 Clutter filter design for ultrasound color flow imaging *IEEE Trans. Ultrason. Ferroelectr. Freq. Control* **49** 204–16

[10] Braack M and Mucha P B 2014 Directional do-nothing condition for the Navier–Stokes equations *J. Comput. Math.* **32** 507–21

[11] Brinkman H C 1949 A calculation of the viscous force exerted by a flowing fluid on a dense swarm of particles *Flow Turbul. Combust.* **1** 1

[12] Caiazzo A, Fernández M A, Gerbeau J-F and Martin V 2011 Projection schemes for fluid flows through a porous interface *SIAM J. Sci. Comput.* **33** 541–64

[13] Caubet F 2013 Instability of an inverse problem for the stationary Navier–Stokes equations *SIAM J. Control Optim.* **51** 2949–75

[14] Caubet F, Dambrine M, Dambrine M, Kateb D and Zakia Timimoun C 2013 A Kohn–Vogelius formulation to detect an obstacle immersed in a fluid *Inverse Problems Imaging* **7** 123

[15] Choulli M, Imanuvilov O and Yamamoto M 2006 Inverse source problem for the Navier-Stokes equations *Preprint Series, Graduate School of Mathematical Sciences, The University of Tokyo*

[16] Ciarlet P G 2013 *Linear and Nonlinear Functional Analysis with Applications* (Philadelphia, PA: SIAM)

[17] de los Reyes J C 2015 *Numerical PDE-Constrained Optimization* (Berlin: Springer)

[18] Dyverfeldt P *et al* 2015 4D flow cardiovascular magnetic resonance consensus statement *J. Cardiovascular Magn. Reson.* **17** 72

[19] Fattouch K, Lancellotti P, Vannan M and Speziale G 2018 *Advances in Treatments for Aortic Valve and Root Diseases* (Berlin: Springer)

[20] Fedele M, Faggiano E, Dedè L and Quarteroni A 2017 A patient-specific aortic valve model based on moving resistive immersed implicit surfaces *Biomech. Model Mechanobiol.* **16** 1779–803

[21] Gröger K 1989 A $W^{1,p}$-estimate for solutions to mixed boundary value problems for second order elliptic differential equations *Math. Ann.* **283** 679–88

[22] Iung B and Vahanian A 2011 Epidemiology of valvular heart disease in the adult *Nat. Rev. Cardiol.* **8** 162–72

[23] John V 2016 *Finite Element Methods for Incompressible Flow Problems* (Berlin: Springer)

[24] Leow C H, Bazigou E, Eckersley R J, Yu A C H, Weinberg P D and Tang M-X 2015 Flow velocity mapping using contrast enhanced high-frame-rate plane wave ultrasound and image tracking: methods and initial *in vitro* and *in vivo* evaluation *Ultrasound Med. Biol.* **41** 2913–25

[25] Li Y L, Hyun D, Abou-Elkacem L, Willmann J K and Dahl J J 2016 Visualization of small-diameter vessels by reduction of incoherent reverberation with coherent flow power Doppler *IEEE Trans. Ultrason. Ferroelect. Freq. Contr.* **63** 1878–89

[26] Martins N F 2015 Identification results for inverse source problems in unsteady Stokes flows *Inverse Problems* **31** 015004

[27] Mayo J R and Leipsic J A 2009 Radiation dose in cardiac CT *Am. J. Roentgenol.* **192** 646–53

[28] Mitusch S, Funke S and Dokken J 2019 Dolfin-adjoint 2018.1: automated adjoints for FEniCS and Firedrake *J. Open Source Softw.* **4** 1292

[29] Mourad H, Hassine M and Malek R 2020 A non-iterative reconstruction method for an inverse problem modeled by an Stokes–Brinkmann equations *J. Korean Math. Soc.* **57** 1079–101